

RESEARCH ARTICLE

10.1002/2016JC012526

Special Section:

Dense Water Formations in the North Western Mediterranean: From the Physical Forcings to the Biogeochemical Consequences

Key Points:

- The AROME-NEMO WMED coupled model was run over HyMeX SOP2 and compared to a uncoupled ocean simulation validated against observations
- Air-sea coupling induces small differences in surface fluxes and in dense water formation (chronology, characteristics, and volumes)
- Fine-scale ocean structures around and interacting with the convective patch are the most sensitive to the air-sea coupling

Supporting Information:

- Supporting Information S1

Correspondence to:

C. Lebeaupin Brossier,
cindy.lebeaupin-brossier@meteo.fr

Citation:

Lebeaupin Brossier, C., F. Léger, H. Giordani, J. Beuvier, M.-N. Bouin, V. Ducrocq, and N. Fourrié (2017), Dense water formation in the north-western Mediterranean area during HyMeX-SOP2 in 1/36° ocean simulations: Ocean-atmosphere coupling impact, *J. Geophys. Res. Oceans*, 122, 5749–5773, doi:10.1002/2016JC012526.

Received 17 NOV 2016







Accepted 22 MAY 2017

Accepted article online 25 MAY 2017

Published online 17 JUL 2017

© 2017. American Geophysical Union.
All Rights Reserved.

Dense water formation in the north-western Mediterranean area during HyMeX-SOP2 in 1/36° ocean simulations: Ocean-atmosphere coupling impact

Cindy Lebeaupin Brossier¹ , Fabien Léger^{1,2} , Hervé Giordani¹ , Jonathan Beuvier^{3,4} , Marie-Noëlle Bouin^{1,5} , Véronique Ducrocq¹, and Nadia Fourrié¹ 

¹Centre National de Recherches Météorologiques (Météo-France/CNRS, UMR3589), Toulouse, France, ²Now at Laboratoire d'Études en Géophysique et Océanographie Spatiales (CNES/IRD/UPS/CNRS, UMR5566), Toulouse, France, ³Mercator Océan, Ramonville Saint-Agne, France, ⁴Météo-France, Toulouse, France, ⁵Laboratoire d'Océanographie Physique et Spatiale (Ifremer/IRD/UBO/CNRS, UMR6523), IUEM, Plouzané, France

Abstract The north-western Mediterranean Sea is a key location for the thermohaline circulation of the basin. The area is characterized by intense air-sea exchanges favored by the succession of strong northerly and north-westerly wind situations (mistral and tramontane) in autumn and winter. Such meteorological conditions lead to significant evaporation and ocean heat loss that are well known as the main triggering factor for the Dense Water Formation (DWF) and winter deep convection episodes. During the HyMeX second field campaign (SOP2, 1 February to 15 March 2013), several platforms were deployed in the area in order to document the DWF and the ocean deep convection, as the air-sea interface conditions. This study investigates the role of the ocean-atmosphere coupling on DWF during winter 2012–2013. The coupled system, based on the NEMO-WMED36 ocean model (1/36° resolution) and the AROME-WMED atmospheric model (2.5 km resolution), was run during 2 months covering the SOP2 and is compared to an ocean-only simulation forced by AROME-WMED real-time forecasts and to observations collected in the north-western Mediterranean area during the HyMeX SOP2. The comparison shows small differences in terms of net heat, water, and momentum fluxes. On average, DWF is slightly sensitive to air-sea coupling. However, fine-scale ocean processes, such as shelf DWF and export or eddies and fronts at the rim of the convective patch, are significantly modified. The wind-current interactions constitute an efficient coupled process at fine scale, acting as a turbulence propagating vectors, producing large mixing and convection at the rim of the convective patch.

1. Introduction

The north-western Mediterranean Sea is a key location for the thermohaline circulation of the basin. In the Gulf of Lion (GoL), the general circulation in the area is characterized by a cyclonic gyre [Millot, 1999] with three distinct layers, despite a relatively weak stratification: Atlantic Water (AW) in the upper layer, above Levantine Intermediate Water (LIW), itself above Western Mediterranean Deep Water (WMDW). The succession of strong wind situations in winter is well known as the major triggering factor for the Dense Water Formation (DWF) in the western Mediterranean [Schott *et al.*, 1996; Marshall and Schott, 1999]. The DWF interannual variability is strongly controlled by the interannual variability of the winter-integrated buoyancy loss, which is connected to the heat loss variability during the winter [Somot *et al.*, 2016]. A strong buoyancy loss was notably responsible for the exceptional DWF that occurred in the area in winter 2005, in terms of extension and volume of newly formed WMDW [Herrmann *et al.*, 2010]. Indeed, in the north-western Mediterranean Sea region, air-sea fluxes present a large variability in space and time. Intense air-sea exchanges (strong momentum flux, evaporation, and heat loss) notably occur when the mistral and tramontane (northerly and north-westerly wind, respectively) affect the area in autumn and winter. They induce extreme cooling and salting of the surface layer. If the surface water is enough dense, a violent mixing occurs, sometimes reaching the seafloor (2500 m depth). This process is known as deep ocean convection.

The estimation and representation of DWF in ocean model is still challenging. Large uncertainties are notably due to the calculation of the exchanges (heat, freshwater, momentum, and kinetic energy) at the air-sea

interface [Caniaux *et al.*, 2017], which strongly control DWF [Herrmann and Somot, 2008; Herrmann *et al.*, 2010; Carniel *et al.*, 2016; Estournel *et al.*, 2016a; Somot *et al.*, 2016]. From the ocean modeling point of view, the surface forcing can be of two kinds. The first forcing method (“bulk” method) consists in using the atmospheric fields (wind, humidity, air temperature, etc.) produced by an atmospheric model simulation. The air-sea fluxes are then computed in the ocean model using its explicit Sea Surface Temperature (SST) and currents. The second way is done by directly using the surface fluxes from an atmospheric model. This method is called “flux forcing.” These two methods however lead to inconsistency. In the “bulk” method, there are differences in fluxes seen by the ocean and atmospheric models. These differences can be enlarged when different bulk formulations are used in the two component models, especially during strong wind events as the bulk parameterizations show the largest discrepancies in such meteorological conditions [e.g., Lebeaupin Brossier *et al.*, 2008; Olabarrieta *et al.*, 2012; Brodeau *et al.*, 2017]. In the second case, the inconsistency arises because of differences in SST. Besides, the ocean feedbacks are generally not taken into account in the fluxes calculation and during the atmospheric model integration. Indeed, a constant initial SST field throughout the simulation is generally used in high-resolution short-range numerical weather prediction models. This was proved to lead to significant errors in the representation of air-sea fluxes during intense events [Rainaud *et al.*, 2016; Ricchi *et al.*, 2016]. Ocean-atmosphere coupled system permits the calculation of the surface fluxes consistently in the ocean and the atmosphere, taking jointly their dynamics into account.

Furthermore, intense fluxes at the air-sea interface are associated with fine-scale intermittent processes in and above [below] the two boundary layers. Such processes are frequent in the north-western Mediterranean subbasin: mesoscale atmospheric systems, storms, wind jets, surface temperature variations, diurnal cycle or gradients linked to eddies, filaments or upwelling [downwelling], low-salinity lenses. To better understand and represent such fine-scale and short-term intense exchanges, the development of ocean-atmosphere coupled system at high-resolution is needed. Such system permits at the same time to accurately solve the mesoscale systems in the two compartment models and to interactively update the near-surface solutions and the exchanges between them. During intense weather events, ocean-atmosphere coupling generally tends to improve the air-sea fluxes and to finally moderate the corresponding atmospheric or oceanic responses. For example, in the studies of Lebeaupin Brossier *et al.* [2009] and Small *et al.* [2011, 2012] over the Gulf of Lion and Ligurian Sea, coupling induces in the ocean component less cooling and less mixing compared to an uncoupled run. But, these two studies only focus on short strong wind events in summer or autumn when the north-western Mediterranean stratification is high. Carniel *et al.* [2016] investigated the coupling (including atmosphere, ocean, and waves) impact on a DWF event in the northern Adriatic Sea using the COAWST system [Warner *et al.*, 2010] at high-resolution (7 km for the atmosphere and 1 km for the ocean [and waves]). They notably showed that the ocean-atmosphere coupling improves the results in particular the total heat flux, by taking into account the dynamic SST prediction in the system. Overall, they concluded that coupling ocean and atmosphere even in a subregion of the model domain may significantly change the circulation and water mass characteristics even in a wider area and can strongly affect the volume of water involved in the densification and its contribution in the deep sea ventilation. Several studies in the Mediterranean already highlight that taking waves into account significantly modify the representation of the atmosphere stability, the wind, the ocean cooling, and mixing [Renault *et al.*, 2012; Ricchi *et al.*, 2016; Carniel *et al.*, 2016]. Indeed, waves play a significant role on the surface roughness length and on the turbulent flux estimation [Janssen, 2004]. The momentum flux parameterization is a key parameter for the three components, as it intervenes in the air-sea, air-waves, and waves-sea exchanges. Moreover, waves strongly modify the upper ocean turbulence [Craig and Banner, 1994; Ardhuin and Jenkins, 2006], and thus can interplay with convection and DWF.

To validate ocean-atmosphere coupled models, simultaneous and colocalized observations of the two boundary layers are also needed. The HyMeX project (Hydrological cycle in the Mediterranean Experiment) [Drobinski *et al.*, 2014] investigates the hydrological cycle in the Mediterranean region. The second Special Observations Period (SOP2) over the north-western Mediterranean area in February–March 2013 [Estournel *et al.*, 2016b] was dedicated to the documentation of the DWF. One objective of the field campaign was to better understand the fine-scale processes involved in the DWF and ocean deep convection, in particular the intense air-sea interactions role and feedbacks. Several atmospheric and ocean platforms were deployed in the north-western Mediterranean Sea during SOP2: aircraft with turbulent measurements,

pressurized boundary layer balloons, radio-soundings, drifting buoys, profiling floats, gliders, XBTs and CTDs from several ships in the area, etc. This observation data set represents a challenging opportunity to identify the coupled processes and small-scale ingredients leading to DWF.

The objective of this study is to evaluate the role of coupled processes in terms of air-sea exchanges and of DWF rates, characteristics and extent, taking benefit of the dense data collection obtained during the SOP2. To do so, two numerical experiments are compared: the AROME-NEMO WMED coupled run and an ocean-only (uncoupled) simulation run with NEMO-WMED36 alone. This latter run was forced by air-sea fluxes extracted from the AROME-WMED real-time forecasts [Fourrié et al., 2015], where the ocean is only seen in the form of a SST analysis updated daily to compute the surface fluxes. This can be seen as a classical flux-forced approach. The reference ocean-only simulation was chosen after a large comparison and validation against HyMeX SOP2 observations done in Léger et al. [2016], where it was shown as the most realistic run in terms of dense water mass characteristics and formation chronology from a sensitivity study to initial conditions, despite a low initial stratification inducing a wide convective patch.

The numerical coupled system and the two experiments are presented in details in section 2. Section 3 analyzes the air-sea interactions at fine scale. The sensitivity of DWF to the coupling is then evaluated in section 4, before focusing on mesoscale ocean features and coupled processes role in section 5. Finally, summary and concluding remarks are given in section 6.

2. Numerical Experiments

2.1. The Coupled System: AROME-NEMO WMED

The AROME-NEMO WMED coupled system combines the nonhydrostatic convective-scale numerical weather prediction system of Météo-France, AROME [Seity et al., 2011] and the ocean model NEMO [Madec and the NEMO team, 2008].

2.1.1. The Atmospheric Model

The atmospheric model configuration is AROME-WMED [Fourrié et al., 2015]. AROME-WMED has a 2.5 km horizontal resolution and cover the whole western Mediterranean Sea (Figure 1a). It has 60 vertical η -levels ranging from 10 m above the ground to 1 hPa. AROME-WMED uses a 1 moment microphysical parameterization [Pinty and Jabouille, 1998; Caniaux et al., 1994], which takes into account five classes of hydrometeors (cloud liquid water, cloud ice, rain, snow, and graupel). The vertical turbulent transport in the boundary layer is represented by two schemes: an eddy diffusivity part based on a prognostic turbulent kinetic energy parameterization following Cuxart et al. [2000] and a dry thermal and shallow convection mass flux scheme following Pergaud et al. [2009]. Thanks to its resolution, the deep convection is explicitly resolved in AROME-WMED. The radiative schemes are the six spectral bands scheme from Fouquart and Bonnel [1980] for short-wave radiation (SW) and the Rapid Radiative Transfer Model (RRTM) [Mlawer et al., 1997] for long-wave radiation (LW). The surface scheme in AROME-WMED is SURFEX [Masson et al., 2013]. Each grid mesh

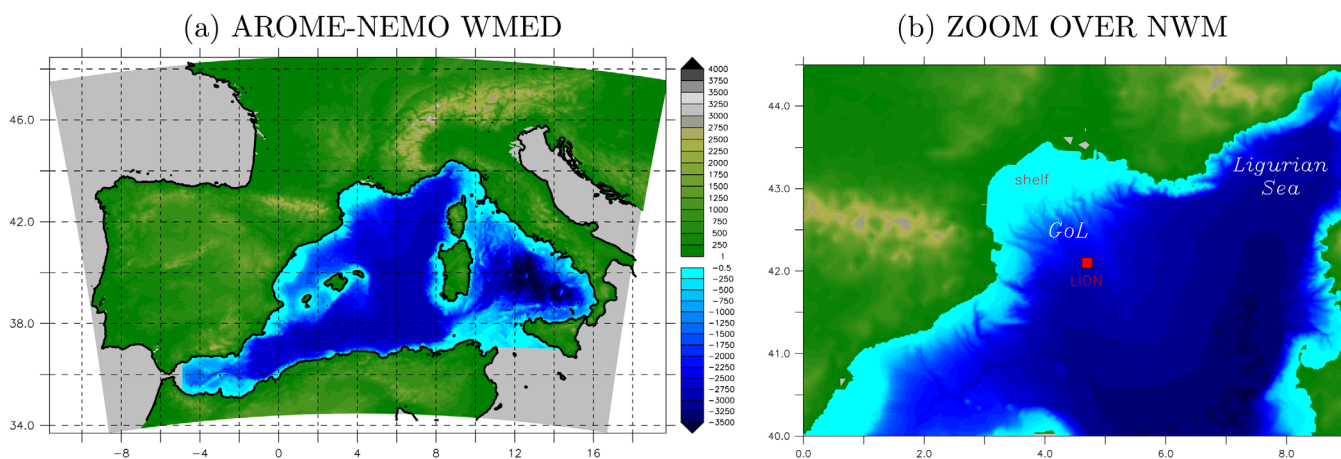


Figure 1. (a) AROME-NEMO WMED domain: AROME-WMED topography (in green) and NEMO-WMED36 bathymetry (in blue). The gray areas are the uncoupled marine zones. (b) Details of the north-western Mediterranean area. The red square indicates the Lion surface buoy and mooring line location.

is split into four tiles: land, towns, sea, and inland waters (lakes and rivers). Output fluxes are weight averaged inside each grid box according to the fraction occupied by each respective tile, before being provided to the atmospheric model. The Interactions between Soil, Biosphere, and Atmosphere (ISBA) parameterization [Noilhan and Planton, 1989] with two vertical layers inside the ground is activated over land tile. The Town Energy Budget (TEB) scheme used for urban tiles [Masson, 2000] simulates urban microclimate features, such as urban heat islands. Concerning inland waters, the Charnock [1955]’s formulation is used. The sea surface fluxes parameterization used by AROME-WMED/SURFEX is described in section 2.1.3.

The atmospheric lateral boundary conditions come from the 10 km resolution ARPEGE [Courtier et al., 1991] global operational forecasts with an hourly frequency.

2.1.2. The Ocean Model

The ocean compartment model is NEMO-WMED36 [Lebeaupin Brossier et al., 2014] with a horizontal resolution of 1/36° over an ORCA grid (Figure 1a). In the vertical, 50 stretched z-levels are used. The vertical level thickness is 1 m in surface and around 400 m for the last levels (i.e., at 4000 m depth). The model has two radiative open boundaries: one west boundary at ~4.8°W (60 km east of the Strait of Gibraltar), one south boundary across the Sicily Channel (~37°N). The Strait of Messina between Sicily and continental Italy is closed. The horizontal eddy viscosity coefficient is fixed to $-1 \times 10^9 \text{ m}^2 \text{ s}^{-1}$ for the dynamics (velocity) with the use of a bi-Laplacian operator. The TVD scheme is used for tracer advection in order to conserve energy and enstrophy [Barnier et al., 2006]. The vertical diffusion is performed by the standard turbulent kinetic energy model of NEMO [Blanke and Delecluse, 1993], and in case of instabilities, a higher diffusivity coefficient of $10 \text{ m}^2 \text{ s}^{-1}$ [Lazar et al., 1999] is used to parameterize convection (see more details in Appendix A). The filtered free surface of Roulet and Madec [2000] is used to keep the sea volume constant. A no-slip lateral boundary condition is applied and the bottom friction is parameterized by a quadratic function with a coefficient depending on the 2-D mean tidal energy [Lyard et al., 2006; Beuvier et al., 2012]. The runoffs are prescribed from a climatology [Beuvier et al., 2010] and applied in surface.

2.1.3. The Coupling Interface and Air-Sea Exchanges

The coupling interface is the SURFEX-OASIS interface [Voldoire et al., 2017] which involves SURFEX and the OASIS3-MCT coupler [Valcke et al., 2013]. This interface manages the exchanges of heat, water and momentum between the ocean and the atmosphere (Figure 2). The corresponding fluxes at the air-sea interface—the solar heat flux Q_{sol} , the nonsolar heat flux Q_{ns} , the freshwater flux F_{wat} , and the momentum flux (or wind stress) $\vec{\tau}$ —are computed only once within SURFEX taking into account near-surface atmospheric and oceanic parameters and their evolutions, following the radiative schemes and the bulk parameterization, and are used consistently in AROME-WMED and NEMO-WMED36,

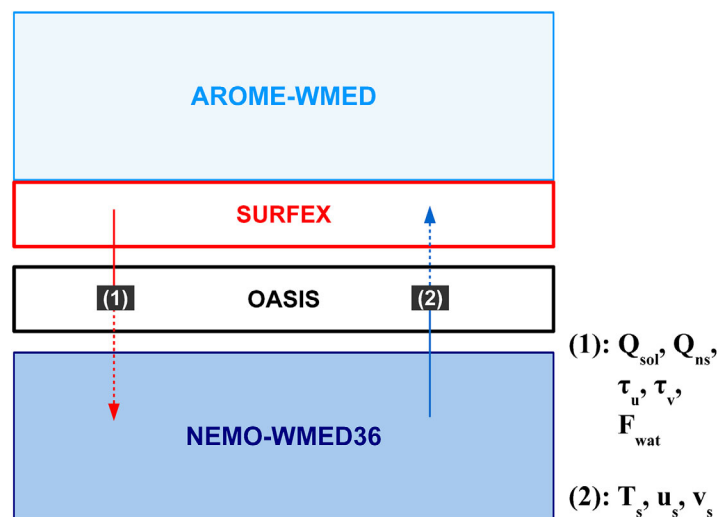


Figure 2. Description of the exchanges between the different components of the AROME-NEMO WMED coupled system.

$$Q_{sol} = (1 - \alpha)SW_{down}, \quad (1)$$

$$Q_{ns} = LW_{down} - \epsilon\sigma T_s^4 - H - LE, \quad (2)$$

where SW_{down} and LW_{down} are the incoming short-wave (solar) and long-wave (infrared) radiative heat fluxes, respectively. H and LE are the sensible and latent heat fluxes, respectively, calculated by the ECUME sea surface turbulent flux bulk parameterization [Belamari, 2005; Belamari and Pirani, 2007]. They depend on the wind speed and air-sea gradients of temperature and humidity, respectively. α is albedo, ϵ is emissivity, and σ is the Stefan-Boltzman constant. T_s is the Sea Surface Temperature (SST).

$$F_{wat} = E - P_l - P_s, \tag{3}$$

where E is evaporation, corresponding to LE/\mathcal{L} , \mathcal{L} is the vaporization heat constant. P_l and P_s are liquid and solid precipitation in surface, respectively (directly coming from AROME to SURFEX).

$$\vec{\tau} = (\tau_u, \tau_v) = \rho_a C_D (U_a - U_s)(\vec{U}_a - \vec{U}_s), \tag{4}$$

where \vec{U}_a is the wind at the lowest atmospheric level (~ 10 m). C_D is the drag coefficient calculated by the ECUME sea surface turbulent fluxes parameterization. ρ_a is the air density.

\vec{U}_s is the ocean near-surface horizontal current, and with T_s , they are here the only oceanic parameters needed to compute the air-sea exchanges, and thus transferred to SURFEX (Figure 2). In return, SURFEX transfers the sea surface fluxes values to OASIS for NEMO.

The coupling only applies on the western Mediterranean Sea: The Atlantic Ocean, the Adriatic Sea, and the western Ionian Sea are uncoupled. In these areas (gray marine zones in Figure 1a), SST comes from the SURFEX (AROME-WMED) initial state (i.e., the surface analysis at 00UT each day) and remains constant during 24 h, and, horizontal current is considered as null.

2.2. Sensitivity Experiments

The coupled run (CPL, Table 1) is compared to an ocean-only simulation (NEMO-WMED36 in the forced mode) named IMAP and validated in Léger *et al.* [2016].

IMAP begins on 1 September 2012 and runs till 15 March 2013 (Table 1). The boundary conditions come from the PSY2V4R4 daily analyses of Mercator-Océan averaged monthly. The PSY2 operational system [Lellouche *et al.*, 2013] has a $1/12^\circ$ horizontal resolution and covers the Northeast Atlantic Ocean, the North and Baltic Seas, and the Mediterranean Sea. The initial conditions were built with the PSY2V4R4 analyze of 1 August 2012 combined with the analyzed fields of the MOOSE campaign over the north-western Mediterranean Sea. The MOOSE campaign took place from 18 July to 5 August 2012 on board of the R/V *Le Suroit*. The analyzed fields, built in the frame of the ASICS-Med project, cover a domain between 40°N and 12°E . They are obtained with an optimal interpolation of observations from CTD profiles in addition to profiling floats (ARGO type), gliders and also SST from satellite radiometers. A numerical sensitivity study on initial conditions using NEMO-WMED36 proves that the ASICS-MOOSE initial conditions are the most accurate to well represent DWF and thermohaline characteristics during HyMeX-SOP2 [Léger *et al.*, 2016]. IMAP is driven at the air-sea interface by the net heat ($Q = Q_{sol} + Q_{ns}$), freshwater (F_{wat}), and momentum fluxes ($\vec{\tau}$) taken each day from the AROME-WMED hourly real-time forecasts, for ranges +1 to +24 h. This means that the SST used to calculate the IMAP surface forcing is the AROME-WMED SST analyses over the whole domain (see the next section and Rainaud *et al.* [2016] for the complete description of the AROME-WMED SST analyses) and that the momentum flux computation takes no horizontal current into account. In IMAP, the Sea Surface Salinity (SSS) is relaxed toward the monthly PSY2V4R4 SSS analyses.

The coupled run, named CPL, starts on 15 January 2013, from the same ocean state than obtained in IMAP for that day. The ocean open-boundary conditions and runoffs are the same as in IMAP, i.e., the monthly averaged PSY2V4R4 analyses provided by Mercator Océan and the Beuvier *et al.* [2010]'s climatology, respectively. The SSS relaxation is turned off in CPL. From the ocean point of view, CPL is a continuous run (NEMO-WMED36 restarts each day from the ocean state of the previous day), whereas the atmospheric component (AROME-WMED) is rerun each day at 00UTC, from initial atmospheric conditions coming from the AROME-WMED analyses (Figure 3). The coupling frequency is 1 h and the interpolation method used by OASIS is bilinear.

Table 1. Description of the Numerical Experiments^a

Name	Begin	End	IC	BC	SURF
IMAP	1 Sep 2012	15 Mar 2013	MOOSE-ASICS + PSY2 Summer 2012	PSY2 (monthly)	Forced mode AROME-WMED forecast (fluxes, 2.5 km, 1 h)
CPL	15 Jan 2013	15 Mar 2013	Restart from IMAP 15 Jan 2013	PSY2 (monthly)	Coupled with AROME-WMED (2.5 km) 1 h frequency

^aIC stands for initial conditions, BC for boundary conditions, and SURF for surface conditions.

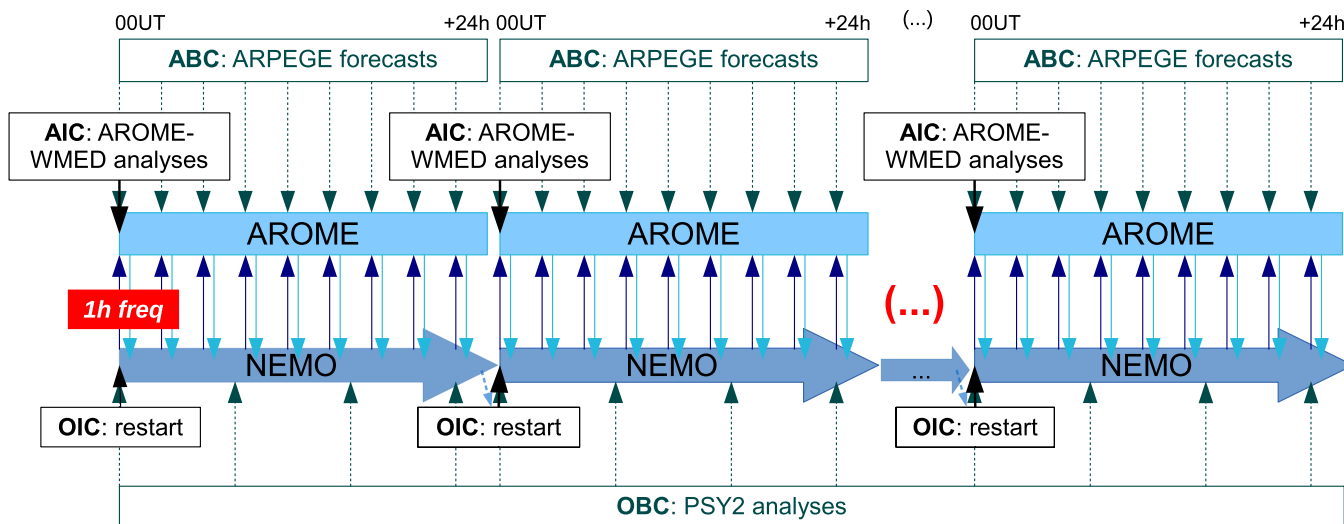


Figure 3. Numerical setup for the CPL experiment. ABC [OBC] stands for atmospheric [ocean] boundary conditions and AIC [OIC] for atmospheric [ocean] initial conditions.

The two experiments run without any assimilation, neither in the ocean model nor in the atmospheric model for what concerns CPL.

3. Air-Sea Interface

In this part, we compare the air-sea exchanges computed in CPL and in AROME-WMED real-time forecast (which later drives the IMAP simulation). As the main differences come from the SST used to compute the turbulent fluxes, we evaluate in the following section the SST fields used by AROME-WMED forecast and those simulated by the CPL experiment.

3.1. AROME-WMED Forecast Versus CPL SST

In AROME-WMED real-time forecasts, the SST used is the 00UT analysis obtained in two steps. First, a 2-D optimal interpolation (CANARI scheme) [Taillefer, 2002] of in situ data is done using the previous 3 hourly analysis as the first guess and using a correlation length of 200 km. Every 3 h, about 20–25 buoy and ship observations are assimilated over the AROME-WMED Mediterranean domain [Rainaud et al., 2016]. This analyzed SST field (SST_a) is secondly blended with the daily OSTIA product (SST_o) [Donlon et al., 2012] to obtain a final analysis [$SST_f = (1 - \alpha)SST_a + \alpha SST_o$ with $\alpha = 0.05$]. The OSTIA SST is provided each day at 06UT with a global coverage on $1/20^\circ$ -resolution grid and integrates various satellite data using an observation window of 36 h centered at 12UT on the previous day. Finally, the effective resolution of the SST analysis is ~ 50 – 100 km and, for the day D, the analysis integrates satellite-based observations since 18UT of D-3, with blending. In addition, there is no SST evolution during the forecast, meaning the SST is kept constant to the 00UTC analysis.

In CPL, the SST is prognostic (solved by NEMO-WMED36) and evolves interactively according to the surface fluxes with a 1 h frequency.

Figure 4 shows an illustration of these SST fields, with a comparison to the MyOcean L3S SST satellite product [Buongiorno et al., 2012] for 1 day well observed (2 March 2013) of the SOP2. This figure shows that:

1. The Northern Current path is very well simulated in CPL but brings too warm AW. The AW path is also visible in the AROME-WMED SST analysis thanks to data assimilation in the eastern part, but not well seen in the western part. This is probably due to the large variability of the current in this area [Conan and Millot, 1995; Millot, 1999], with eddies and meanders which detach or enter in the shelf area, and make the current path difficult to capture considering the low effective resolution (around 50–100 km) and despite the data assimilation.

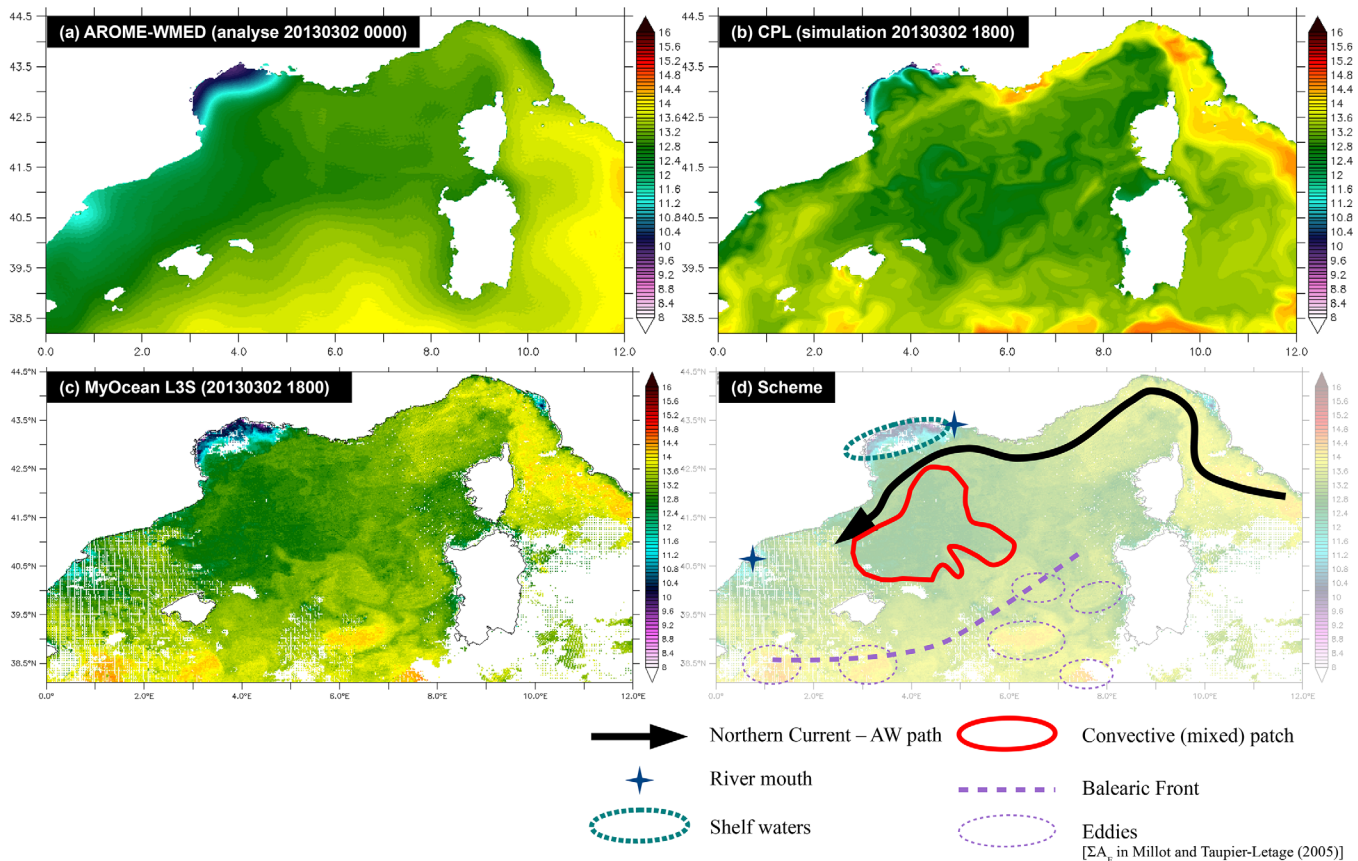


Figure 4. SST fields on 2 March 2013 18UT. (a) AROME-WMED forecast corresponding to the analysis at 00UT, (b) CPL simulation, (c) MyOcean L3S supercollocated product (resolution: 0.01°; source: <http://hoc.sedoo.fr>, restricted access) and (d) schematic view of the SST patterns and related processes according to the L3S SST field in Figure 4c.

2. In CPL, the Balearic Front is thin and warm eddies—as described in *Millot and Taupier-Letage* [2005]—are simulated in the southern part. In the AROME-WMED analysis the Balearic front is smooth and no eddy can be seen.
3. The cold (and fresh) shelf waters [*Estournel et al.*, 2003] are well visible in the two SST fields, but the offshore convective patch is only clearly seen in CPL.

Due to the limitation of the direct satellite observation in winter, the comparison done here can only be qualitative. Nevertheless, these difference patterns can generally be found when considering the SOP2 (Figure 5a). The Northern Current is explicitly reproduced in CPL but too warm (+0.5°C), whereas it is not well captured in the AROME-WMED analysis especially in the western part. The smooth Balearic front and the lack of the cold offshore convective patch in AROME-WMED lead to a too high SST in the southern part of the north-western Mediterranean area.

In addition, the interactive evolution of the SST in CPL allows to take into account the diurnal variation (in case of calm situation) or rapid surface cooling (response to mistral), whereas it is not the case in the real-time AROME-WMED forecasts (see supporting information Figure S1).

To conclude, the coupling permits to take into account the SST small-scale patterns and rapid variations for the heat fluxes (and evaporation) computation. More important is that there is a balance between SST and fluxes in CPL. The fluxes computed in AROME-WMED real forecast (and driving IMAP) are indeed unbalanced with the ocean and have also a relatively low resolution.

3.2. Sea Surface Fluxes

The time series of the net heat flux, freshwater flux, and wind stress during SOP2 are shown in Figure 6. They are almost similar between CPL and the AROME-WMED forecast.

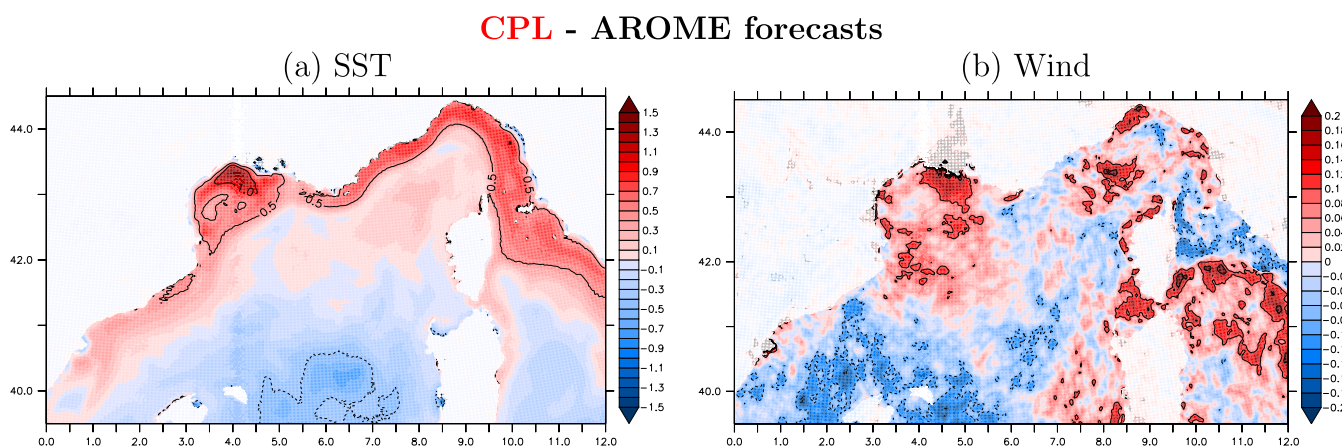


Figure 5. Mean differences during SOP2 in (a) SST (K, contours every 0.5 K) and (b) wind speed (m s^{-1} , contours every 0.1 m s^{-1}) at the first atmospheric level ($\sim 10 \text{ m}$), between CPL and the AROME-WMED operational forecasts.

The largest differences in net heat flux are found during strong wind events when a slightly lower net heat loss is produced in CPL. At the same periods, the wind stress is lower in CPL, whereas the freshwater flux (dominated by evaporation) is the same between CPL and AROME-WMED (IMAP). The total differences after 2 months of integration are finally of 660 W m^{-2} for the net heat flux (corresponding to -6.9% of the AROME-WMED [IMAP] total heat loss during SOP2), of $7 \times 10^{-4} \text{ kg m}^{-2} \text{ s}^{-1}$ for the freshwater flux but reductions of both E (-2.5%) and precipitation $P_I + P_s$ (-0.5%) in CPL (not shown), and of -0.5 N m^{-2} (-3.8%) for the stress (Figure 6).

The mean flux fields during SOP2 in the two experiments as their mean differences are presented in Figure 7. It shows that even if the differences on average over the north-western Mediterranean Sea are small (Figure 6), the local differences can be large. The two experiments evidence the large heat loss in the area induced by strong mistral and tramontane. The patterns are almost similar; however, the differences in net heat flux show two areas responding differently to coupling. In CPL, compared to AROME-WMED, less heat is lost in the southern offshore area, whereas the heat loss is larger along the coasts. These two areas correspond well to the differences found in the SST fields (Figure 5a), with the CPL SST higher along the Northern Current and over the shelf area linked to the AW (warm surface water) circulation. It produces larger turbulent heat fluxes and thus a larger net heat loss (lower net heat flux). On the other hand, CPL SST is lower offshore near the Balearic Islands and thus induces a lower net heat loss. Even if the freshwater flux fields are more noisy, as precipitation occurs very locally, the difference patterns show similitudes with the net heat flux differences (Figure 7c). Indeed, evaporation is generally reduced in the open-sea convective area whereas it is increased in the coastal area, in particular over the shelf. These patterns are related to the differences in the SST field between AROME-WMED forecasts and CPL (Figure 5a). Wind stress is slightly changed but differences show a reduction of the momentum flux in the center and southern part of the north-western Mediterranean area (Figure 7c). On the contrary, an increase is found close to the Italian coasts and over the GoL shelf. These differences do not correspond to the differences in low-level wind shown in Figure 5b. They seem to be linked to differences in SST (Figure 5a), with a small increase in the wind stress where the SST is largely higher in CPL. Elsewhere, the stress is reduced because of the reduction due to the surface current (see equation (4), as U_s is null in AROME-WMED forecasts), and also offshore because of a colder surface (Figure 5a), probably linked to a stabilization of the atmospheric boundary layer and thus to a reduction of the near-surface wind (Figure 5b) [Pullen *et al.*, 2006].

4. Dense Water Formation Sensitivity to Coupling

4.1. Mixed-Layer Depth

Figure 8 presents the mean and maximum Mixed-Layer Depths (MLDs) from a density criteria (MLD is defined as the depth with a density gradient of 0.01 kg m^{-3} with the surface) during SOP2 for the two experiments. It shows that they have a quite similar convective patch, from the GoL to the Ligurian Sea. Although some deep mixed profiles were observed in the Ligurian Sea during SOP2, the convection in

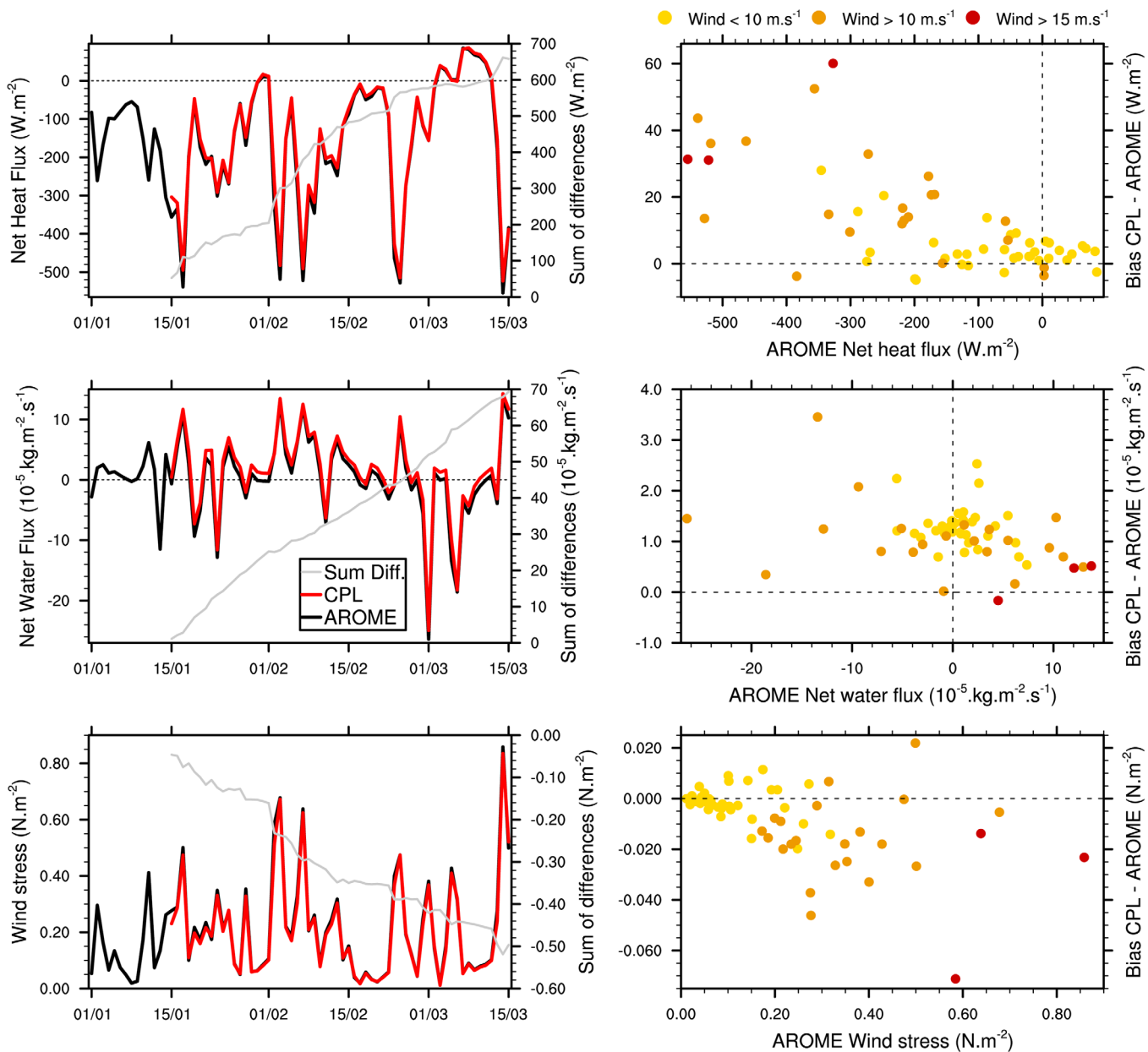


Figure 6. (left) Daily time series of the net heat flux (W m^{-2}), of the freshwater flux ($\text{kg m}^{-2} \text{s}^{-1}$) and of the momentum flux (N m^{-2}) intensity over the north-western Mediterranean Sea in AROME-WMED forecasts (used to compute the surface forcing for IMAP) and in CPL. The gray lines are the sums since 15 January of the differences between CPL and AROME-WMED (scales on the right). (right) Daily differences in the net heat flux, the freshwater flux and the momentum flux between CPL and AROME-WMED as a function of the daily flux values in AROME-WMED. The color indicates the range of the corresponding daily mean wind speed in AROME-WMED forecasts over the north-western Mediterranean Sea.

IMAP is overestimated in this area due to a low initial stratification [Léger *et al.*, 2016]. The mean MLD is generally lower in CPL than in IMAP (by 300–500 m, corresponding to ~ -15 to -40%), except over the shelf area where it is larger by ~ 50 m (~ 2 times larger than IMAP). The same difference patterns are found when considering the maximum MLD. The two distinct responses for the shelf and the offshore regions correspond directly to the differences in surface fluxes shown previously: in CPL, the mixing is lower in the GoL because of a lower net heat loss (and evaporation and stress), whereas it is larger over the shelf due to a larger net heat loss. The largest differences between CPL and IMAP MLDs (up to -2000 to -2400 m) are found at the rim of the deep convective patch area. In fact, they correspond to some grid meshes where deep convection does not occur at all in CPL. The comparison to observations is done using floats (ARGO) and CTD profiles and the spatiotemporally colocalized simulated profiles: 213 profiles, located offshore, are

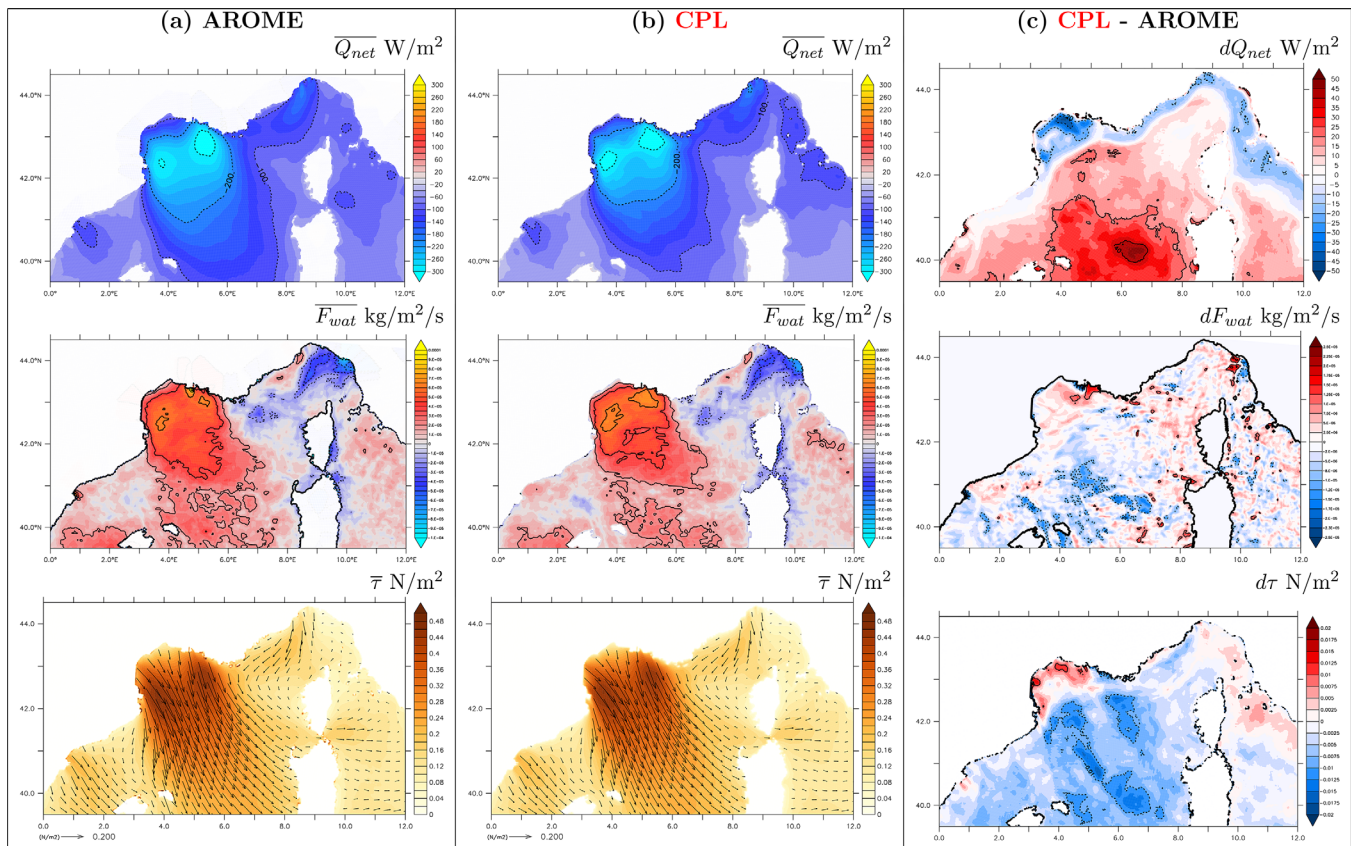


Figure 7. Mean net heat flux (W m^{-2}), freshwater flux ($\text{kg m}^{-2} \text{s}^{-1}$) and momentum flux (N m^{-2}) during SOP2 in (a) AROME-WMED forecasts and (b) in CPL, and (c) mean differences between CPL and IMAP.

considered and the observed MLD is obtained with the same density criteria. The MLD distribution (Figure 9) confirms that the number of very deep-mixed simulated profiles ($\text{MLD} > 1750 \text{ m}$) is lower and closer to observations in CPL than IMAP (see also supporting information Figure S2). However, for the other MLD classes, the number of profiles is closer to the observations in IMAP. Figure 9 also highlights that during SOP2 either the water column is stratified with MLD shallower than 250 m, or, the whole column is mixed and the MLD is deeper than 1750 m.

To further evaluate the differences in the MLD fields, we computed skill scores as classically done to qualify mesoscale prediction of severe events (see *Ducrocq et al.* [2002] and Appendix B) using the 213 “observed” MLDs as verification (see supporting information Figure S2). Indeed, these skill scores measure the ability of the high-resolution models to reproduce the deep [extreme] convection event with a good intensity, size, and location and allow to evaluate more finely the reliability of the two simulations for the deep ocean convection. Done for several MLD thresholds (Figure 10), CPL shows an improvement of the deep convective patch representation: deeper the threshold is, better CPL is compared to IMAP. For the threshold of 1750 m depth, the HSS shows a good representation of the deep mixing event for the two experiments, better than a random prediction. The HSS is 0.49 for CPL and 0.41 for IMAP proving that the localization of the convective patch is a little better in the coupled simulation. The FBIAS is 1.41 for IMAP against 1.21 for CPL, which shows the overestimation of the mixed patch in both simulations, but more significant in IMAP. The strong ability to create more events above the threshold leads to a higher and better POD (0.72) but a higher and worse FAR (0.49) in IMAP than in CPL (respectively 0.71 and 0.41). On the contrary, for the smaller thresholds the skill scores present better results for IMAP.

4.2. Water Mass Characteristics

The θ/S characteristics over the north-western Mediterranean area strongly change during SOP2 (Figure 11). After 2 months, both simulations show a cooling and an increase in salinity for the ocean upper layers

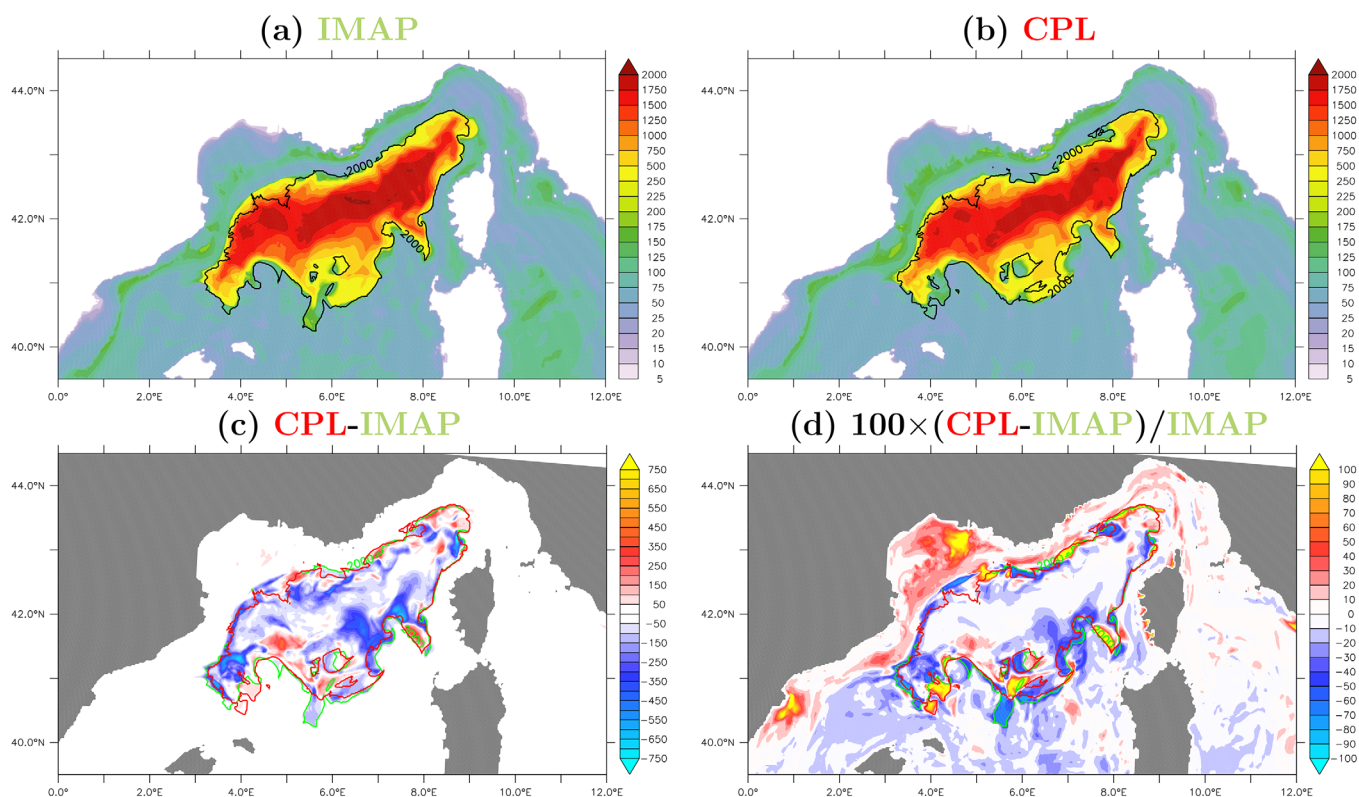


Figure 8. Mean mixed-layer depth (colors, m) from a density criteria in (a) IMAP and (b) CPL. (c) Absolute (in meters) and (d) relative (in %) differences in the mean MLD between CPL and IMAP. The contours indicate the area where the maximum MLD simulated during SOP2 is larger than 2000 m depth (green for IMAP and red for CPL in Figures 8c and 8d).

(0–350 m). The LIW are less pronounced in mid-March than in mid-January, with a decrease in salinity and temperature at 350–600 m depth, corresponding to LIW mixing with the upper layer water. The WMDW shows an increase in salinity (+0.002 psu) and a small increase in temperature below 1500 m depth (+0.005°C), corresponding to the newly formed dense water. CPL and IMAP have similar θ/S characteristics for WMDW, which are only a very little warmer (+0.015°C) and saltier (+0.002 psu) than observed (at 1950 m depth). Considering that the “observed θ/S diagram” is an unweighted average over the north-western Mediterranean Sea and over the whole SOP2, i.e., it is built from an inhomogeneous data set in space and time, such differences can be considered as not significant. This result is confirmed by the mean vertical biases against the observed profiles from floats obtained using a colocalization in space and time (see supporting information Figure S3) and the biases and standard deviations computed for three layers and considering the whole SOP2 (Table 2). These scores show that the two experiments are very close to each other. The largest differences are found for the upper layers (0–150 m). The mean differences for the whole north-western Mediterranean area between CPL and IMAP is of +0.025°C and +0.03 psu. When only considering the simulated profiles colocalized with (Argo type) floats (unevenly distributed over the area), the differences between CPL and IMAP are of +0.039°C and –0.005 psu in the 0–150 m layer (Table 2). The differences are +0.007°C and –0.002 psu when only the profiles colocalized with CTDs are considered (Table 2). For the three layers (0–150 m, 150–600 m, 600 m to bottom), the two experiments are close to observations with very small biases and standard deviations (Table 2). The only significant modification is finally found for temperature in the upper layer (0–150 m), where the coupling shows an improvement.

The two simulations are finally compared to the data collected at Lion (4.7°E–42.1°N, Figure 1b) by the MOOSE mooring line and the surface buoy (SST doi:10.6096/HyMeX.LionBuoy.Thermosalinograh.20100308 and SSS doi:10.6096/MISTRALS-HyMex-MOOSE.1025) in Figure 12. The observed time series of temperature and salinity between 1 February and 15 March 2013 show three phases (Figure 12): first a “mixing” phase progressively reaching the seafloor and characterized by salinity and temperature increases at 1500 m

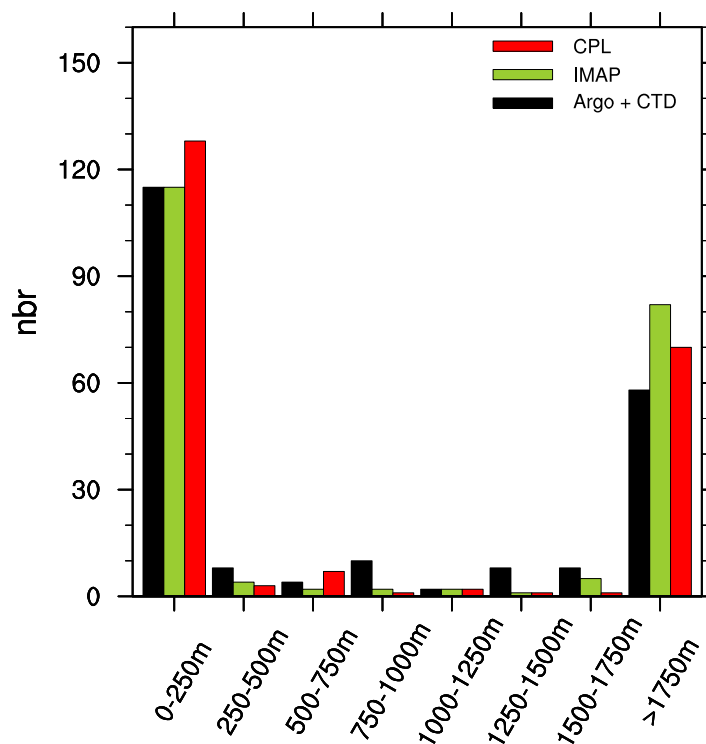


Figure 9. Distribution (number of profiles) of the MLD (m) from density in situ profiles (floats [ARGO type] and R/V *Le Suroit* CTDs) during SOP2 in the north-western Mediterranean and spatiotemporally colocalized in the two simulations IMAP and CPL.

“mixed” phase, IMAP and CPL simulate increases in θ/S at 1500 and 2000 m depth which are not observed. The largest differences between IMAP and CPL clearly appear from IOP24, during the restratification period, for all the levels considered, but in particular with different behavior in the very upper layer (see section 5.2).

4.3. Dense Water Volumes and Formation Rates

The time series of the dense water volumes in the north-western Mediterranean Sea are presented in Figure 13 for the two simulations. Almost the same evolutions of dense water volume are found, with similar chronologies. However, progressively along SOP2, CPL produces less water denser than 29.11 and 29.12 kg m^{-3} than IMAP. On 15 March 2013, compared to IMAP, the volume of water denser than 29.11 kg m^{-3} is decreased in CPL by 4%, and of water denser than 29.12 kg m^{-3} by 49%. The 29.11 kg m^{-3} production rate, computed by only considering the volume increasing phases during the period, is 2.59 Sv in IMAP and 2.38 Sv (−8%) in CPL, and, the 29.12 kg m^{-3} production rate is 0.77 Sv in IMAP and 0.56 Sv (−27%) in CPL. On the other hand, the volume of water denser than 29.13 kg m^{-3} is larger in CPL than in IMAP, but stays low (up to 320 km^3 on 3 March against 50 km^3 for IMAP, Figure 13c). This dense water is in fact a signature of the dense water production in the shelf area, where the surface fluxes are larger in CPL (see section 5). *Waldman et al.* [2016] estimated the integral formation rate for the whole north-western Mediterranean Sea using an *Observing System Simulation Experiment* method to be $2.3 \pm 0.5 \text{ Sv}$ for winter 2012–2013. They also obtained a volume of water with density $\rho > 29.11 \text{ kg/m}^3$ of $17.7 \pm 0.9 \times 10^4 \text{ km}^3$ on April 2013. The coupled run with lower volumes (Figure 13) and formation rates is thus slightly in better agreement with the estimation of *Waldman et al.* [2016] than IMAP.

In summary, at the scale of the north-western Mediterranean area, the DWF directly responds to the surface flux modifications due to coupling, i.e., a change in the SST field seen by AROME-WMED. In the offshore area, a lower heat loss, evaporation and wind stress lead to a decrease in DWF. On the contrary over the shelf area, the increase of the turbulent fluxes induces a larger production of dense water.

depth (3 February) and at 2000 m depth (8–9 February). The LIW appears already mixed at the beginning of February. Then a “mixed” phase is visible with small changes in S and θ , ended by a convective event marked by a new increase in θ/S (27–28 February). Finally, a restratification period is seen with a high temporal variability in the observations for all levels and marked in surface by θ diurnal cycles and short decreases in SSS. This restratification period ended by a new convection event from IOP28 on 15 March. The simulations show first a lower variability of the θ/S time series. In surface and at 300 m depth the simulated values are close to observations. Despite initial biases, the two simulations well reproduce the rapid θ/S increases at 1500 m depth (but in advance of 1 day) and at 2000 m depth. During the

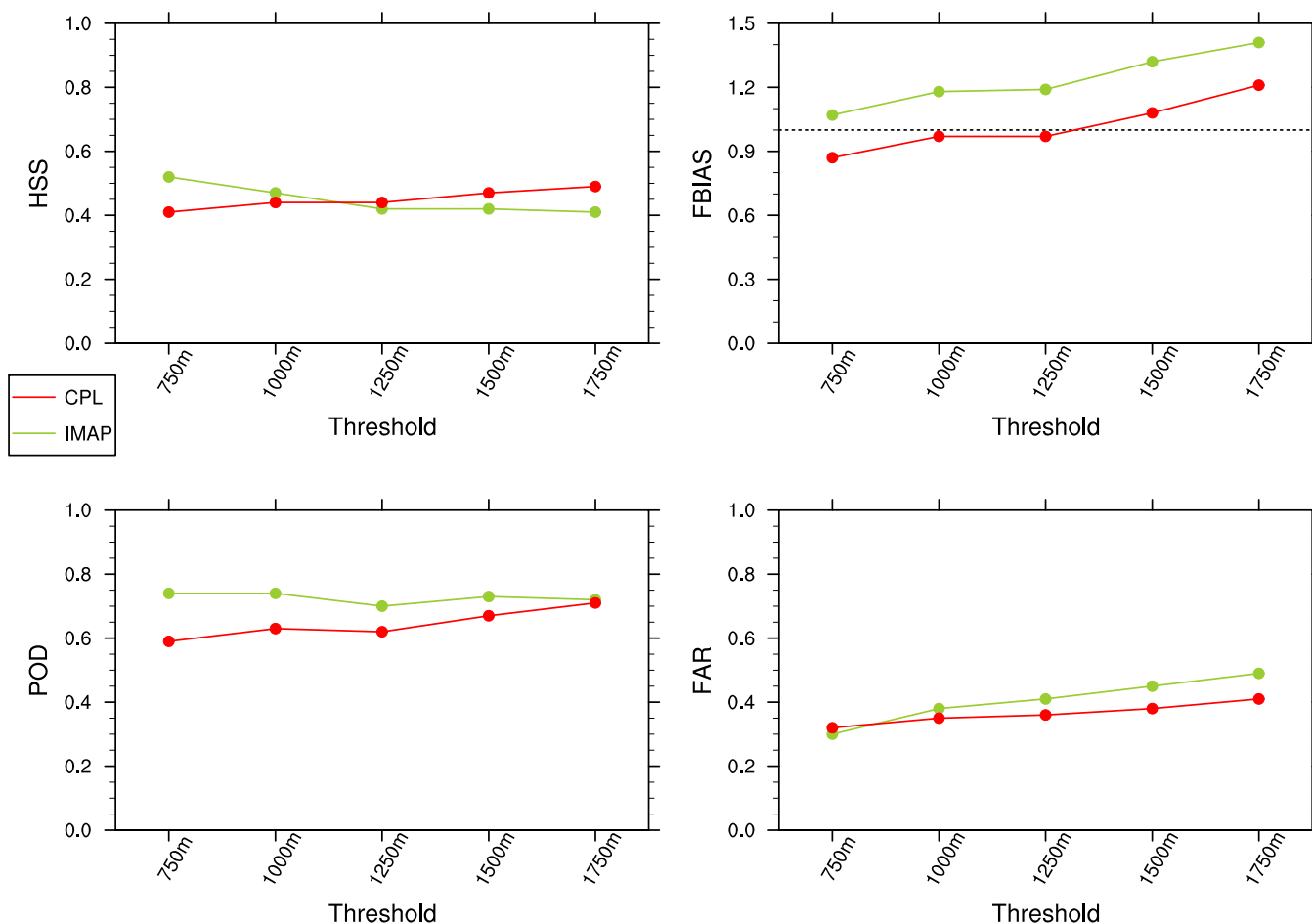


Figure 10. Skill scores (HSS, FBIAS, POD, and FAR, see Appendix B) for IMAP and CPL obtained when compared to observed MLD in density in situ profiles (floats [ARGO type] and R/V *Le Suroit* CTDs) and considering various MLD thresholds.

5. Mesoscale Features

The general circulation at the basin scale is very similar between IMAP and CPL (see supporting information Figure S4). But, as preliminary indicated by the modification of the convective patch perimeter (Figure 8) and by a larger shelf DWF in CPL (Figure 13), the fine-scale ocean circulation and structures seem to be very sensitive to the air-sea coupled processes. The objective of this section is to illustrate some fine-scale structures response to coupling and to preliminary examine in CPL some coupled processes acting at the rim of the convective zone.

5.1. Shelf DWF and Export

Figure 14 shows an instant view (2 March 2013) of the DWF in the two experiments. It highlights that, at that time, new dense water is formed over the shelf and offshore in both simulations. In the offshore zone, the 29.12 kg m^{-3} isopycnal has almost the same patterns and homogeneous characteristics ($\theta = 12.9^\circ\text{C}$, $S = 38.45\text{--}38.5 \text{ psu}$), but it is less deep and covers a wider area in IMAP than in CPL, indicating that a more intense deep convection occurred in IMAP. The deep eddies at $4.4^\circ\text{E}\text{--}40.9^\circ\text{N}$ and at $4.7^\circ\text{E}\text{--}41.5^\circ\text{N}$, containing and propagating deepward and southward the new dense water, are the most significantly changed. Over the shelf, the new dense water is constrained along the coast in IMAP at upper level. Its temperature is below 11°C and its salinity is below 38 psu. In CPL, the shelf dense water is warmer ($\sim 11.6^\circ\text{C}$) and saltier (38.1–38.2 psu) than in IMAP and flows between the surface and 75 m depth along meanders. At the Cap Creus canyon ($3.5^\circ\text{E}\text{--}42.3^\circ\text{N}$), it overflows. When it leaves the shelf, this dense water volume is rapidly integrated to the WMDW within the offshore mixed patch and diffused.

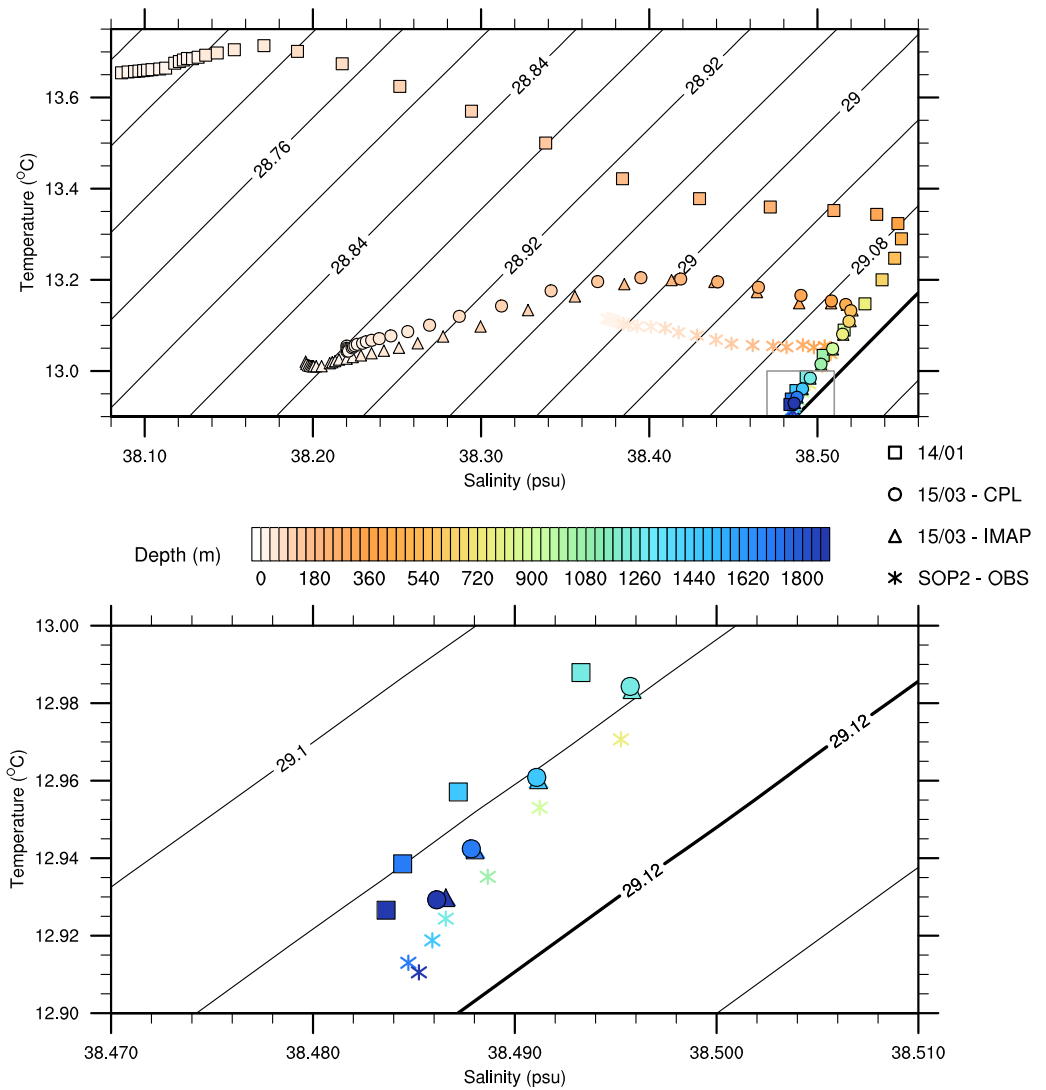


Figure 11. (top) θ/S diagram averaged in the north-western Mediterranean area before the convection (14 January 2013, squares) and at the end of SOP2 (15 March 2013) for the two experiments (triangles for IMAP and circles for CPL). (bottom) Zoom for the WMDW (dashed rectangle in the top panel). The mean θ/S diagram from in situ floats [ARGO type] averaged over SOP2 is indicated with stars.

Table 2. Biases and Standard Deviations Against Argo Floats and CTD Profiles for Potential Temperature (θ), Salinity (S), and Density (ρ)

Argo Floats	θ (°C)				S (psu)				ρ (kg m ⁻³)			
	0–150m	150–600m	600–2000 m	Total	0–150m	150–600 m	600–2000 m	Total	0–150 m	150–600 m	600–2000 m	Total
IMAP												
Bias	-0.120	-0.003	0.013	-0.004	-0.028	-0.13×10^{-3}	2.98×10^{-3}	-0.68×10^{-3}	3.18×10^{-3}	0.51×10^{-3}	-0.30×10^{-3}	0.24×10^{-3}
Std dev	0.268	0.124	0.042	0.115	0.110	0.043	0.010	0.042	0.101	0.030	0.005	0.034
CPL												
Bias	-0.081	0.012	0.014	0.005	-0.033	2.90×10^{-3}	2.56×10^{-3}	-0.57×10^{-3}	-8.57×10^{-3}	-0.20×10^{-3}	-0.99×10^{-3}	-1.46×10^{-3}
Std dev	0.237	0.132	0.047	0.109	0.112	0.041	0.005	0.042	0.100	0.027	0.005	0.037
CTD profiles												
IMAP												
Bias	-0.048	-0.059	0.017	-0.003	-0.039	-0.026	-0.31×10^{-3}	-8.53×10^{-3}	-0.020	-7.88×10^{-3}	-3.78×10^{-3}	-5.95×10^{-3}
Std dev	0.255	0.165	0.073	0.120	0.113	0.056	0.020	0.045	0.110	0.043	0.004	0.036
CPL												
Bias	-0.041	-0.054	0.022	0.001	-0.041	-0.027	0.33×10^{-3}	-8.57×10^{-3}	-0.024	-9.56×10^{-3}	-4.20×10^{-3}	-6.80×10^{-3}
Std dev	0.225	0.159	0.075	0.114	0.105	0.056	0.021	0.044	0.101	0.042	0.004	0.034

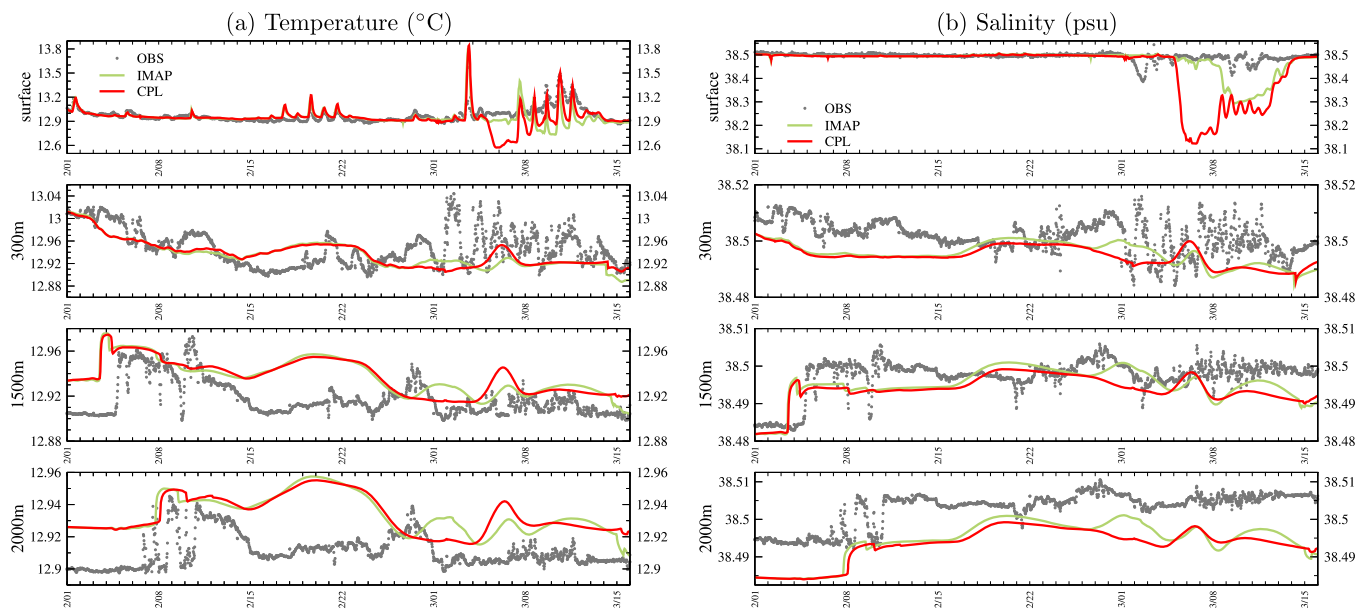


Figure 12. Lion buoy and mooring [4.7°E–42.1°N]: simulated and observed temperature (°C) and salinity (psu) in surface, at 300 m depth, at 1500 m depth and at 2000 m depth.

So, it appears that the local modifications of the surface fluxes due to coupling strongly constrain the circulation over the shelf. As a result, the dense shelf water volume is strongly increased (6 times larger for water denser than 29.13 kg m^{-3} in CPL) and overflows in canyon. The dense shelf water salinity is significantly increased (+0.2 to +0.3 psu) because of the larger evaporation and of a larger mixing (related to the larger wind stress) in the area (Figure 7) and the temperature is higher in CPL than in IMAP (+0.6°C) despite a larger net heat loss locally ($+20 \text{ W m}^{-2}$, Figure 7), but related to a larger mixing and (warm) AW intrusion (see Figure 4 [for the same date] and Figure 15).

5.2. Offshore Eddy

The comparison to the Lion surface buoy and mooring data set previously showed that the two simulations are very similar in terms of chronology and close to the in situ observations in surface, except at the end of SOP2 (5–13 March 2013) when restratification occurs. CPL shows negative biases in temperature and salinity, maximum on 6 March. As highlighted by the profile time series (Figure 12), these biases are due to too cold and fresh water in the 0–50 m layer coming at Lion. Almost the same cold bias is found in IMAP, but with a delay of ~ 4 days. Indeed, Figure 15 presents the SST and SSS maps for 6 March 2013. It shows that the fresh and cold water intrusion is due to a very fine eddy reaching the Lion buoy in CPL (Figure 15b), whereas the cold and fresh eddy is located 10 km south of the moored buoy in IMAP (Figure 15a). Elsewhere, the CPL SST is higher. Compared to IMAP, the CPL SSS is larger inside the GoL gyre and over the shelf, but lower in the Balearic front. Below 50 m depth, the water column stays well mixed. From 9 March, a diurnal warming occurs in the very thin (0–5 m) near-surface layer due to a radiative heating larger than the turbulent heat loss (Figure 12). Then, between 13 and 15 March, as a new mixing event occurs, both simulations have surface temperature and salinity in agreement with observed values (Figure 12).

5.3. Wind Energy Flux

In the following, the fine-scale coupled dynamical processes related to DWF are preliminarily evaluated. For that purpose, rather than the buoyancy flux largely controlled by the atmospheric fields (not shown), the surface Wind Energy Flux (WEF) which quantifies the kinetic energy flux injected in to the ocean by the wind stress at the air-sea interface [Giordani *et al.*, 2013] is computed. Indeed, the WEF is the dot product of the wind stress $\vec{\tau} = (\tau_u, \tau_v)$ with the surface horizontal ocean velocity $\vec{U}_s = (u_s, v_s)$,

$$WEF = \vec{\tau} \cdot \vec{U}_s = \tau_u u_s + \tau_v v_s. \quad (5)$$

When the WEF is positive, the wind stress and the surface current have the same direction and thus the atmosphere can increase the ocean mean kinetic energy; and conversely when the WEF is negative

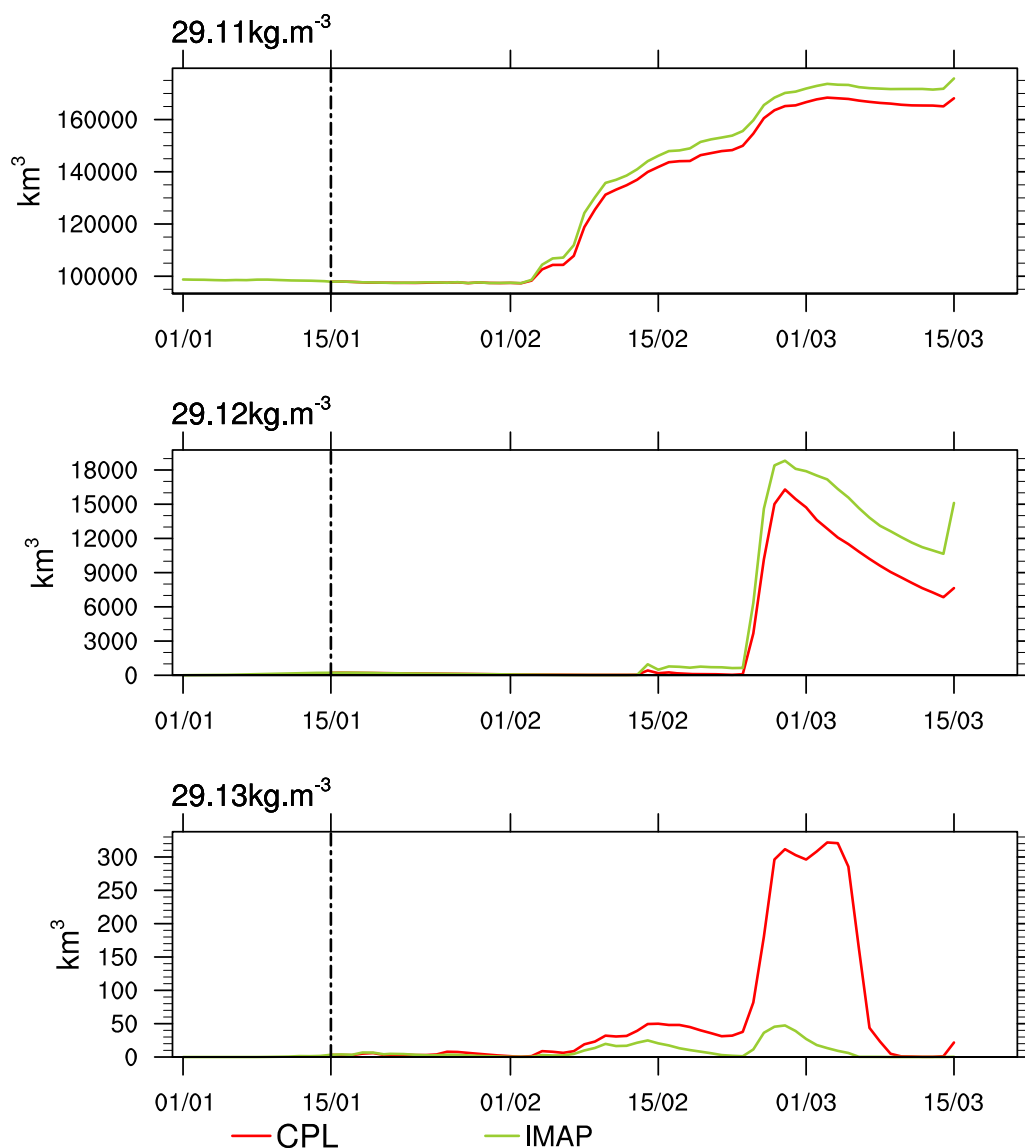


Figure 13. Time series of the dense water volumes (km^3): water denser than (a) 29.11 kg m^{-3} , (b) 29.12 kg m^{-3} , and (c) 29.13 kg m^{-3} .

[Giordani et al., 2006]. The WEF is examined in the CPL experiment as the relationship between wind/stress/currents/mixing is explicit thanks to coupling.

Figure 16 presents the daily-mean surface fluxes and circulation, the mixed layer depth from the turbulence (where $K_z \geq 5 \text{ cm}^2 \text{ s}^{-1}$) and density criteria, the daily mean WEF and the vertical velocity for 7 February 2013 corresponding to the mistral/tramontane event of IOP21c and just before the convection reach the seafloor. It shows that the WEF maxima are located at the rim of the mixed patch. These maxima correspond to the locations where the Northern Current and the cyclonic circulation are in the same direction as the north/north-westerly wind (stress) and thus are the places where the surface wind energy is efficiently injected into the currents inside the mixed layer. The vertical response to the WEF forcing is a production of vertical velocity. The largest intensities of the vertical velocity (Figures 16d–16f, up to 800 m d^{-1} in absolute value) are indeed found to be close to the locations with high WEF (for example in the western [3.7°E – 42°N] and southern [4.5°E – 41.5°N] parts of the mixed (dense) patch, Figure 16c). It also shows the permutation of downward motion with upward motion, with a characteristic size of $\sim 10 \text{ km}$. The injected kinetic energy participates to the destabilization of the front and is a key parameter for the turbulent mixing [Giordani et al., 2013]. It adjusts the “mixing” layer with here a rapid and larger increase of the MLD from a turbulent criteria, in particular at the western and southern boundaries (Figure 16b) of the convective zone.

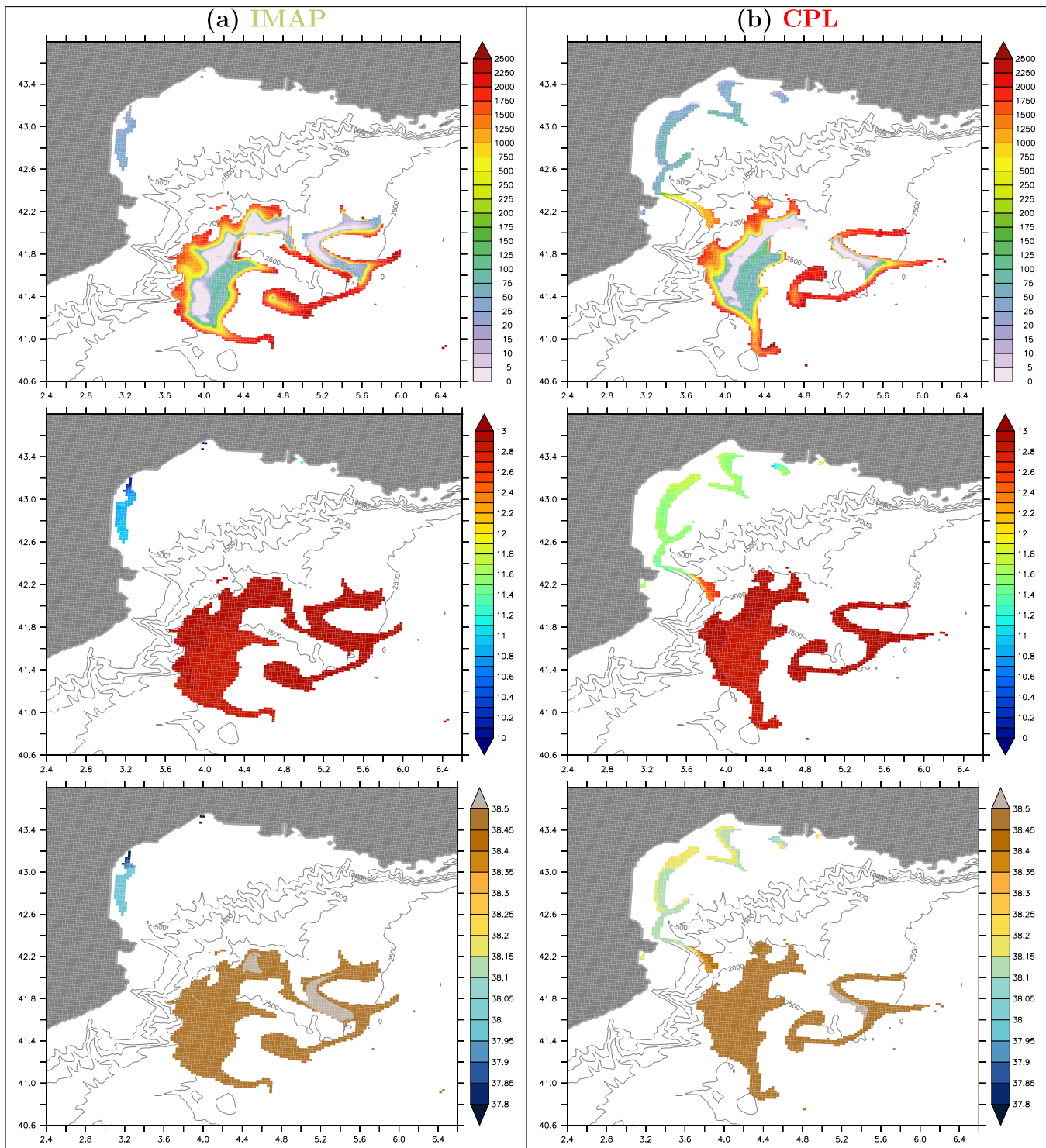


Figure 14. 29.12 kg m^{-3} isopycnal surface depth (m, top), temperature ($^{\circ}\text{C}$, middle) and salinity (psu, bottom) simulated on 2 March 2013 12UT by (a) IMAP and (b) CPL.

This indicates a conversion of the kinetic energy into turbulence and vertical motion in the frontal zone and thus illustrates the major role of the wind/stress/current interactions at the rim of the convective patch on turbulent mixing. Nevertheless, additional analyses must be conducted to further investigate the mechanical coupled processes acting on convection and DWF, as suggested by *Giordani et al.* [2017].

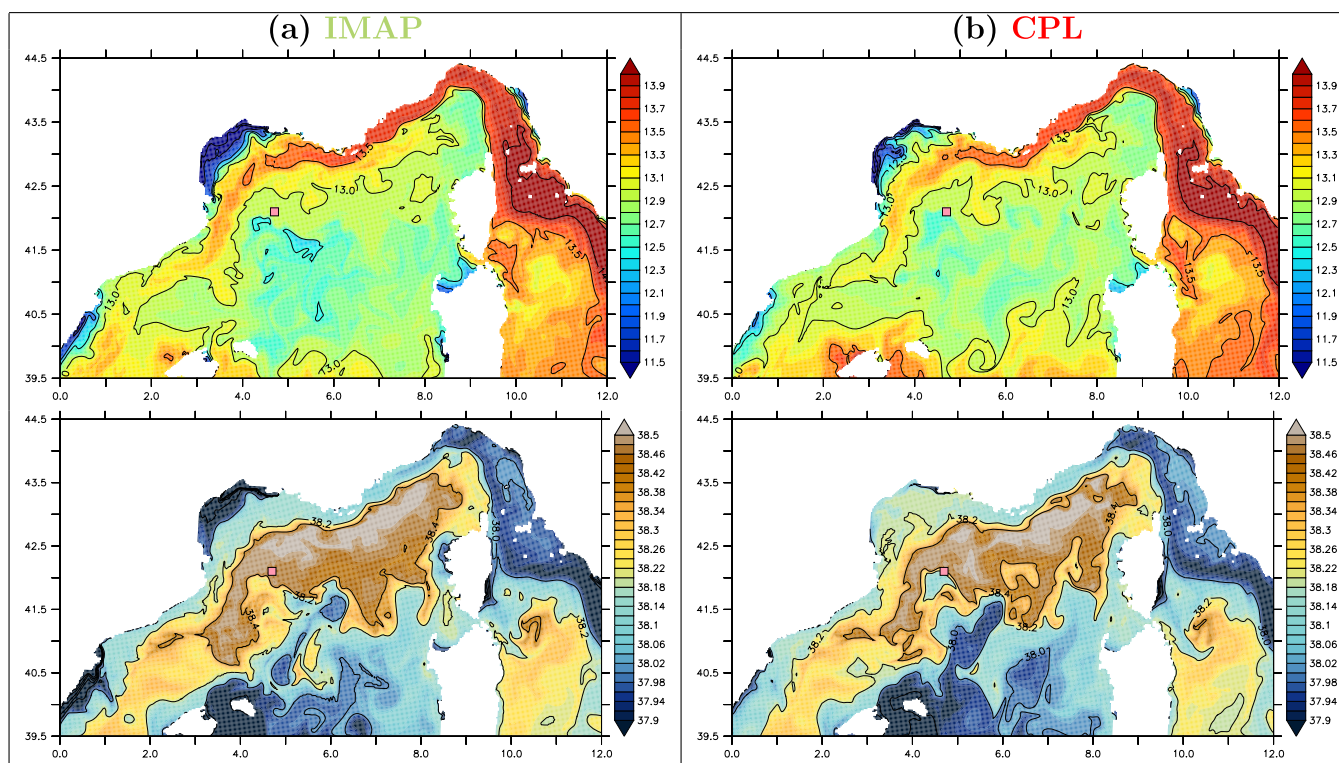


Figure 15. Sea surface temperature ($^{\circ}\text{C}$, top) and Salinity (psu, bottom) simulated on 6 March 2013 00UT in (a) IMAP and (b) CPL. The pink square indicates the Lion buoy location.

6. Summary and Conclusion

This study evaluates the mesoscale air-sea coupling impacts on DWF. For that, the coupling between the NEMO-WMED36 ocean model and the AROME-WMED numerical weather prediction (atmospheric) model was developed and run over 2 months covering the HyMeX SOP2. The AROME-NEMO WMED coupled simulation (CPL) was compared to an ocean-only simulation (IMAP) forced by AROME-WMED real-time forecasts. A comparison to observations collected during the field campaign was also done and constitutes a first validation of the high-resolution air-sea coupled system for ocean purposes. This validation shows that the two simulations represent in a realistic way the winter 2013 convection (MLD and chronology) and DWF event (volume and characteristics) that was sampled by the field campaign.

The results, summarized in Figure 17, show that, first, the air-sea fluxes are slightly decreased on average in the coupled simulation. The fluxes are in fact modified in relationship with the change in the SST field seen by SURFEX and AROME. In CPL, the heat loss and evaporation are increased over the shelf and in the coastal area, whereas a decrease is found elsewhere, notably over the GoL. The modifications of the wind stress are small.

As a consequence, the offshore DWF is reduced in CPL and the deep convective patch is slightly smaller corresponding to an improvement when compared to the MLD deduced from in situ profiles, but the thermal characteristics are not significantly changed. From the categorical scores computed considering MLD thresholds, it appears that the two simulations are almost similar in term of deep convective (mixed) patch. But, considering the dense network of observations obtained during the field campaign, there is a high potential of such skill scores when comparing ocean model abilities in representing the deep convection intensity, size, and location that could be useful, notably in a context of intercomparison. Over the shelf, the coupled simulation shows a high sensitivity of the mixing to coupling and a larger (but limited) production of dense water ($\rho \geq 29.13 \text{ kg m}^{-3}$). Despite the ocean model limitations due to the horizontal resolution of $1/36^{\circ}$, the z coordinate levels and the hydrostatic assumption, CPL produces an overflow of the shelf DWF

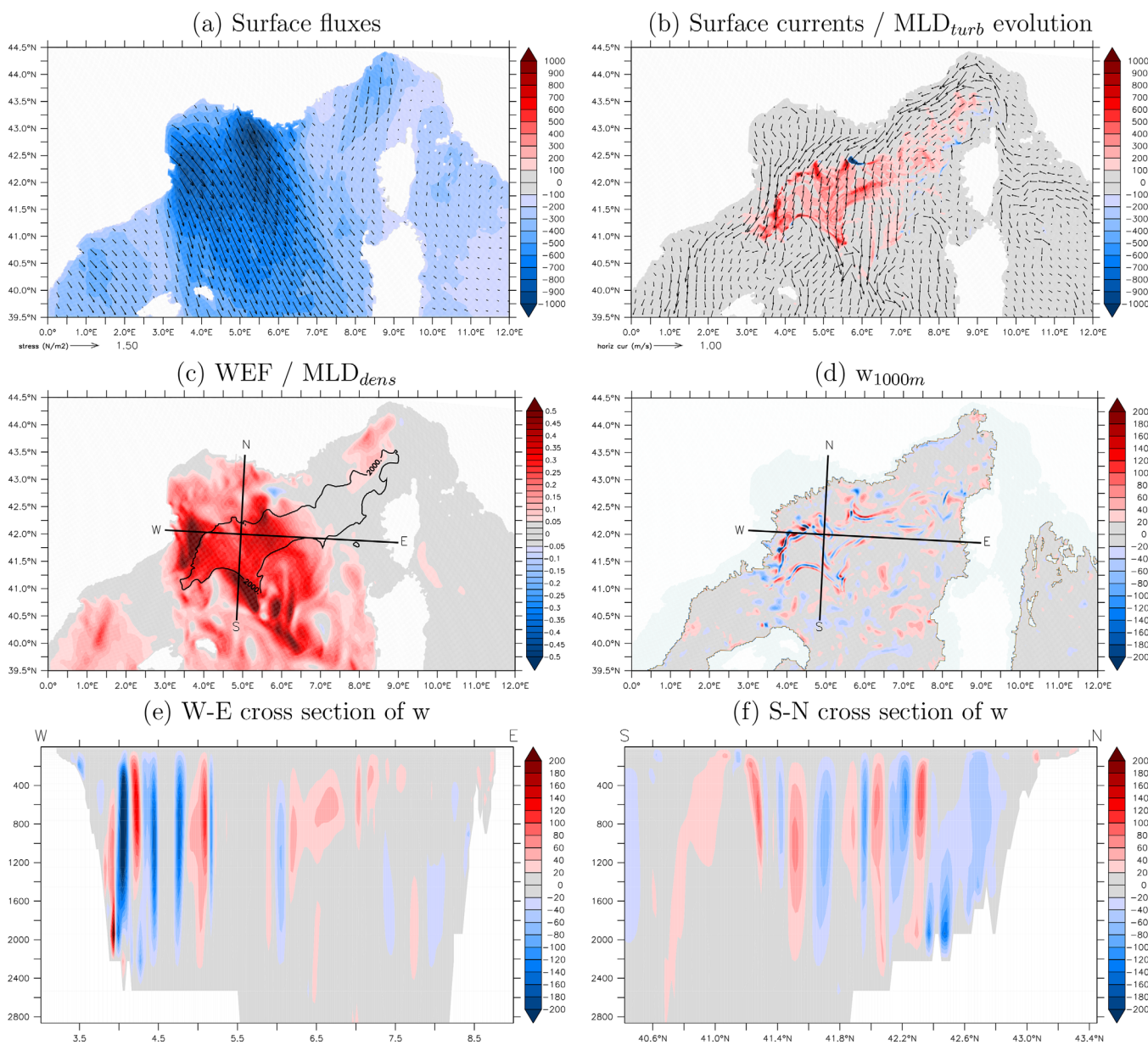


Figure 16.7 February 2013 (IOP21c) in CPL: (a) daily mean net heat flux (colors, W m^{-2}) and wind stress (arrows, N m^{-2}). (b) Surface current (arrows, m s^{-1}) and daily evolution of the MLD from a turbulence criteria (colors, in m/d). (c) Daily mean WEF (colors, $\text{N m}^{-1} \text{s}^{-2}$). The black contour indicates where the daily maximum MLD from a density criteria reaches 2000 m. (d) Daily mean vertical velocity (w , in m/d) at 1000 m depth. (e, f) Vertical cross sections (thick solid black lines in Figures 16c and 16d) of the daily mean vertical velocity (in m/d).

in the Cap Creus Canyon whose occurrence (referred as “cascading”) is also suggested by some observations [Estournel *et al.*, 2016b; Testor *et al.*, 2017].

The main differences between the coupled and forced simulations are found in the frontal zones, more specifically at the rim of the cyclonic gyre. The fine-scale ocean structures around the mixed patch, like coastal currents, eddies, fronts, and meanders, seem to be very sensitive to the air-sea coupled processes. Precisely, these ocean mesoscale features are in strong interaction with the convective zone, so they can control the 3-D transport of AW and LIW increasing locally the stratification, or, on the contrary, the transport of well-mixed (dense) water columns. In addition, the configuration of the north-western Mediterranean region, with characteristic strong northerly winds with fine jets and a mesoscale ocean circulation marked by numerous fine-scale ocean structures, often leads to optimal wind-current interactions. It results in significant vertical motion at the rim of the convective patch, triggered by the kinetic energy injection

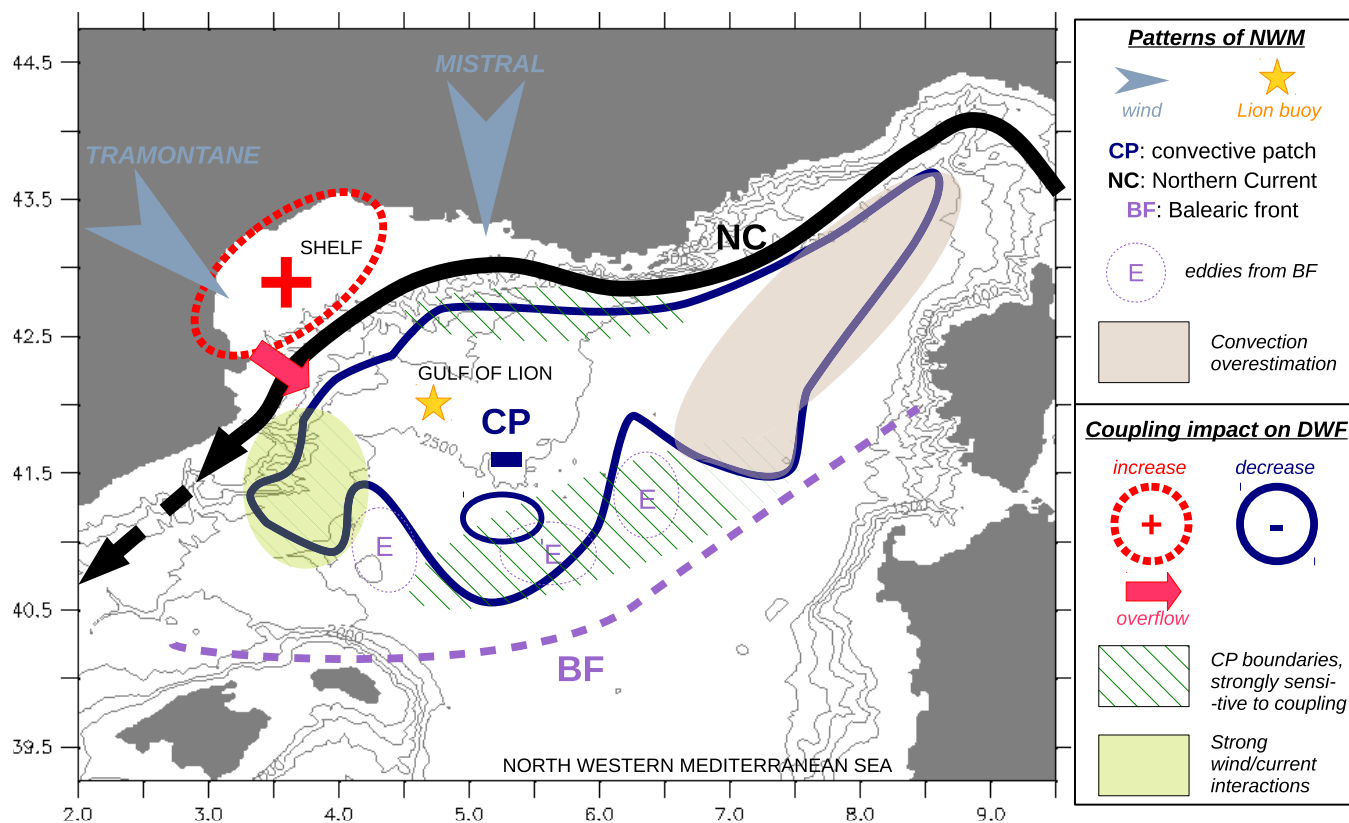


Figure 17. Schematic summary of the ocean-atmosphere coupling impacts on DWF in the north-western Mediterranean Sea during HyMeX SOP2, deduced from AROME-NEMO WMED simulations.

from the atmosphere to the mixing layer and by the front destabilization. This coupled mechanism acts efficiently and at fine-scale as a turbulence propagating vector, producing large mixing and convection.

Even if this result must be further investigated, for example for other case studies and with other coupled models, it already gives the first insights of how coupled processes like mesoscale ocean structures/ strong wind interactions could significantly affect the vertical motion and convection associated with DWF and the thermohaline circulation. The perspective of this work will be to use a potential vorticity approach in order to further analyze the coupled processes between the surface wind and the rim of the cyclonic gyre, because of their strong impacts on the ocean dynamics and dense water formation [Giordani et al., 2017]. Then, a vertical scheme considering the mass flux as in Pergaud et al. [2009], which is under development for ocean, will also be used in order to improve the ocean convection representation in the coupled system. Finally, using a sea state forcing or introducing a wave model in the coupled system will also be considered.

Appendix A: Turbulent Mixing Scheme in NEMO-WMED36

The vertical eddy viscosity A^{vm} and diffusivity A^{VT} coefficients are computed from a TKE turbulent closure model based on a prognostic equation for the turbulent kinetic energy \bar{e} and a closure assumption for the turbulent length scales. This turbulent closure model has been developed by Bougeault and Lacarrère [1989] in the atmospheric case, adapted by Gaspar et al. [1990] for the oceanic case, and implemented in OPA by Blanke and Delecluse [1993] then by Madec et al. [1998] in NEMO.

The time evolution of \bar{e} is the result of the production of \bar{e} through vertical shear, its destruction through stratification, its vertical diffusion, and its dissipation of Kolmogorov [1942] type, which can be numerically written as (k is the vertical coordinate),

$$\frac{\partial \bar{e}}{\partial t} = \frac{A^{vm}}{e_3} \left[\left(\frac{\partial u}{\partial k} \right)^2 + \left(\frac{\partial v}{\partial k} \right)^2 \right] - A^{vT} N^2 + \frac{1}{e_3} \frac{\partial}{\partial k} \left[\frac{A^{vm}}{e_3} \frac{\partial \bar{e}}{\partial k} \right] - C_\epsilon \frac{\bar{e}^{-3/2}}{l_\epsilon}, \tag{A1}$$

$$A^{vm} = C_k l_k \sqrt{\bar{e}}, \tag{A2}$$

$$A^{vT} = A^{vm} / Pr_t, \tag{A3}$$

where e_3 is the level thickness, u and v are the horizontal components of the velocity, N is the local Brunt-Vaisl frequency, l_ϵ and l_k are the dissipation and mixing length scales, Pr_t is the Prantl number which is a function of the Richardson number [see *Blanke and Delecluse*, 1993]. The constants C_k and C_ϵ are set to 0.7 and 0.1, respectively, to deal with vertical mixing at any depth.

The mixing length are obtained by $l_\epsilon = l_k = \sqrt{2\bar{e}}/N$ with an extra assumption concerning their vertical gradient: $\frac{1}{e_3} \left| \frac{\partial l}{\partial k} \right| \leq 1$ with $l = l_k = l_\epsilon$. For that two additional length scales are introduced: $l_{up}^{(k)} = \min(l^{(k)}, l_{up}^{(k+1)} + e_3^{(k)})$ from $k = 1$ to jp_k (i.e., the bottom level) and $l_{dwn}^{(k)} = \min(l^{(k)}, l_{dwn}^{(k-1)} + e_3^{(k-1)})$ from $k = jp_k$ to 1 with $l^{(k)} = \sqrt{2\bar{e}^{(k)}/N^{(k)}}$.

Then $l_k = \sqrt{l_{up} l_{dwn}}$ and $l_\epsilon = \min(l_{up}, l_{dwn})$.

At the surface, $\bar{e} = 60 ||\bar{\tau}||$ with a minimum value of $10^{-4} \text{ m}^2 \text{ s}^{-2}$. At the bottom, \bar{e} is assumed to be equal to the value of the level just above. Cut-offs are applied on \bar{e} , A^{vm} , and A^{vT} with minimum value of $10^{-6} \text{ m}^2 \text{ s}^{-2}$, $10^{-4} \text{ m}^2 \text{ s}^{-1}$, and $10^{-5} \text{ m}^2 \text{ s}^{-1}$ respective minimum values.

The reader is referred to *Bougeault and Lacarrère* [1989], *Gaspar et al.* [1990], and *Blanke and Delecluse* [1993] for a complete description of the TKE vertical mixing scheme and to *Madec et al.* [1998] and *Madec and the NEMO team* [2008] for the implementation.

Furthermore, as the NEMO model is hydrostatic, convection is not explicitly solve in case of static instabilities (when a profile has a low density under a high density). For that purpose, the enhanced vertical diffusion parameterization is used to represent convection. So, in case of unstable conditions, a constant $A^{EVD} = 10 \text{ m}^2 \text{ s}^{-1}$ is added on the vertical eddy coefficient A^{vT} [*Lazar et al.*, 1999].

Appendix B: Skill Scores for Mixed-Layer Depth Evaluation

In a similar manner than *Ducrocq et al.* [2002], we use a 2×2 contingency table (Table A1) considering different thresholds of MLD to compute,

1. The frequency bias $FBIAS = (b+d)/(c+d)$,
2. The probability of detection $POD = d/(c+d)$,
3. The false alarm rate $FAR = b/(b+d)$,
4. The Heidke skill score $HSS = (a+d-T)/(N-T)$,

with $N = a+b+c+d$ the total number of observations (density profiles from floats (ARGO type) and R/V *Le Suroit* CTDs), $T = [(a+c)(a+b) + (b+d)(c+d)]/N$ referring to the expected number of all the correct simulated values with a random simulation. The FBIAS measures the ability of the model to predict the occurrence of the event "over the threshold." The POD describes the ability in representing the size of the event and should be pondered with the FAR, which considers the rate of false detection of the intense event. It does not take into account localization errors. The HSS score measures the ability to predict the event relatively to the accuracy of random simulation.

Table A1. Schematic 2×2 Contingency Table for the Definition of Scores, Given a Threshold thr for the MLD

	Simulation	Simulation
	$< thr$	$\geq thr$
Observation $< thr$	a	b
Observation $\geq thr$	c	d

The occurrence of the event "over the threshold." The POD describes the ability in representing the size of the event and should be pondered with the FAR, which considers the rate of false detection of the intense event. It does not take into account localization errors. The HSS score measures the ability to predict the event relatively to the accuracy of random simulation.

A perfect prediction has FAR equal to 0 and FBIAS, POD, and HSS equal to 1. A random prediction has HSS equal to 0.

Notation

Models and Parameterizations

AROME	application of research to operations at mesoscale.
AROME-WMED	Western Mediterranean configuration of AROME.
ARPEGE	Action de Recherche Petite Echelle Grande Echelle.
ECUME	exchange coefficients from unified multi-campaign estimates.
ISBA	interactions between soil, biosphere and atmosphere.
NEMO	nucleus for European modeling of the ocean.
(NEMO)-WMED36	Western Mediterranean basin configuration of NEMO (1/36° resolution).
OASIS	ocean atmosphere sea ice soil.
OASIS3-MCT	version of OASIS.
PSY2(V4R4)	regional operational NEMO configuration from Mercator Océan (1/12° resolution).
RRTM	rapid radiative transfer model.
SURFEX	surface externalized.
TEB	town energy budget.
TVD	total variance dissipation scheme.

Simulations

CPL	AROME-NEMO WMED coupled simulation.
IMAP	NEMO-WMED36 simulation, initialization with the MOOSE-ASICS analysis and PSY2.

Fields and Constants

α	Albedo.
C_D	Drag coefficient.
ϵ	emissivity.
E	evaporation.
F_{wat}	freshwater flux.
H	sensible heat flux.
\mathcal{L}	latent heat of vaporization.
LE	latent heat flux.
LW	long-wave radiative flux.
LW_{down}	downward long-wave radiative flux.
MLD	mixed-layer depth.
P_l	liquid precipitation.
P_s	solid precipitation.
Q	net heat flux.
Q_{ns}	nonsolar heat flux.
Q_{sol}	solar heat flux.
ρ	ocean density.
ρ_a	air density.
σ	Stefan-Boltzman constant.
S	salinity.
SSS	sea surface salinity.
SST or T_s	sea surface temperature.
SW	short-wave radiative flux.
SW_{down}	downward short-wave radiative flux.
θ	potential ocean temperature.
$\tau_r, \tau_{ur}, \tau_v$	wind stress and components.
U_{ar}, u_{ar}, v_a	near-surface wind and components.

U_s, u_s, v_s surface ocean velocity and components.
 w ocean vertical velocity.
 WEF wind energy flux.

Skill Scores

FAR false alarm rate.
 FBIAS frequency bias.
 HSS Heidke skill score.
 POD probability of detection.

Observations

CTD conductivity-temperature-depth.
 IOP intensive observations period (the reader is referred to Léger *et al.* [2016] for IOP numbers).
 SOP special observations period.
 R/V research-vessel.
 XBT expendable bathythermograph.

Water Masses, Processes, and Locations

AW Atlantic Water.
 DWF dense water formation.
 GoL Gulf of Lion.
 LIW Levantine intermediate water.
 WMDW Western Mediterranean dense water.

Projects

ASICS-Med air-sea interaction and coupling with submesoscale structures in the Mediterranean.
 HyMeX hydrological cycle in the Mediterranean experiment.
 MISTRALS Mediterranean integrated studies at regional and local scales.
 MOOSE Mediterranean ocean observing system for the environment.
 SiMed simulation of the Mediterranean Sea.

References

Arduin, F., and A. D. Jenkins (2006), On the interaction of surface waves and upper ocean turbulence, *J. Phys. Oceanogr.*, *36*(3), 551–557, doi:10.1175/JPO2862.1.

Barnier, B., et al. (2006), Impact of partial steps and momentum advection schemes in a global ocean circulation model at eddy-permitting resolution, *Ocean Dyn.*, *56*(5–6), 543–567, doi:10.1007/s10236-006-0082-1.

Belamari, S. (2005), Report on uncertainty estimates of an optimal bulk formulation for turbulent fluxes, in *Tech. Rep. MERSEA IP Deliverable, D.4.1.2*, 31 pp., Eur. Commission, Brussels, Belgium.

Belamari, S., and A. Pirani (2007), Validation of the optimal heat and momentum fluxes using the ORCA-LIM global ocean-ice model, in *Tech. Rep. MERSEA IP Deliverable, D.4.1.3*, 88 pp., Eur. Commission, Brussels, Belgium.

Beuvier, J., F. Sevault, M. Herrmann, H. Kontoyiannis, W. Ludwig, M. Rixen, E. Stanev, K. Béranger, and S. Somot (2010), Modelling the Mediterranean Sea interannual variability during 1961–2000: Focus on the Eastern Mediterranean Transient (EMT), *J. Geophys. Res.*, *115*, C08517, doi:10.1029/2009JC005950.

Beuvier, J., K. Béranger, C. Lebeaupin Brossier, S. Somot, F. Sevault, Y. Drillet, R. Bourdallé-Badie, N. Ferry, B. Levier, and F. Lyard (2012), Spreading of the Western Mediterranean Deep Water after winter 2005, time-scales and deep cyclone transport, *J. Geophys. Res.*, *117*, C07022, doi:10.1029/2011JC007679.

Blanke, B., and P. Delecluse (1993), Variability of the tropical Atlantic Ocean simulated by a general circulation model with two different mixed layer physics, *J. Phys. Oceanogr.*, *23*, 1363–1388.

Brodeau, L., B. Barnier, S. K. Gulev, and C. Woods (2017), Climatologically significant effects of some approximations in the bulk parameterizations of turbulent air-sea fluxes, *J. Phys. Oceanogr.*, *47*(1), 5–28, doi:10.1175/JPO-D-16-0169.1.

Bougeault, P., and P. Lacarrère (1989), Parameterization of orography-induced turbulence in a meso-beta scale model, *Mon. Weather Rev.*, *117*, 1872–1890.

Buongiorno, N. B., C. Tronconi, A. Pisano, and R. Santorelli (2012), Hugh and ultra-high resolution processing of satellite sea surface temperature data over Southern European Seas in the framework of MyOcean project, *Remote Sens. Environ.*, *129*, 1–16, doi:10.1016/j.rse.2012.10.012.

Caniaux, G., J.-L. Redelsperger, and J.-P. Lafore (1994), A numerical study of the stratiform region of a fast-moving squall line, Part I: General description and water and heat budgets, *J. Atmos. Sci.*, *51*, 2046–2074.

Acknowledgments

This work is a contribution to the HyMeX program (HYdrological cycle in the Mediterranean Experiment, www.hymex.org) through INSU-MISTRALS support, through SiMed (Simulation of the MEDiterranean Sea) transverse axis support and through the ASICS-MED project (Air-Sea Interaction and Coupling with Submesoscale structures in the MEDiterranean, ANR-12-BS06-0003). The authors acknowledge Météo-France for supplying the Lion buoy data set, the MOOSE observatory for supplying the Lion mooring line data set [Principal Investigators: Xavier Durrieu de Madron (UPVD) and Pierre Testor (LOCEAN)], Mercator Océan for supplying the PSY2V4R4 analysis and the HyMeX database teams (ESPRI/IPSL and SEDOO/OMP) for their help in accessing the data. The profiling (ARGO) floats and CTD data set were collected and made freely available by the Coriolis project and programs that contribute to it (<http://www.coriolis.eu.org>). For these latter data, the Principal Investigators of the MOOSE-GE and DeWEX cruises [Laurent Coppola (LOV), Laurent Mortier and Pierre Testor (LOCEAN)] and of the R/V Téthys II and the P/T Le Provence cruises during HyMeX-SOP2 [Isabelle Taupier-Letage (MIO); doi:10.6096/MISTRALS-HyMeX.950] are gratefully acknowledged. The authors gratefully thank Françoise Orain (Météo-France/Centre de Météorologie Spatiale) who produced and provided the quicklooks of several SST satellite products to the HyMeX Operational Center (HOC) website. The authors also thank Thomas Arsouze (ENSTA/LMD) for his help in the development of the NEMO WMED36 configuration and for fruitful discussions about this work. Cindy Lebeaupin Brossier finally acknowledges Aurore Voldoire and Bertrand Decharme (CNRM) for their invaluable help in the AROME-SURFEX-OASIS-NEMO coupled system development.

- Caniaux, G., L. Prieur, H. Giordani, and J.-L. Redelsperger (2017), An inverse method to derive surface fluxes from the closure of oceanic heat and water budgets: Application to the north-western Mediterranean Sea, *J. Geophys. Res. Oceans*, doi:10.1002/2016JC012167, in press.
- Carniel, S., A. Benetazzo, D. Donaldo, F. M. Falcieri, M. M. Miglietta, A. Ricchi, and M. Scavo (2016), Scratching beneath the surface while coupling atmosphere, ocean and waves: Analysis of a dense water formation event, *Ocean Modell.*, *101*, 101–112, doi:10.1016/j.ocemod.2016.03.007.
- Charnock, H. (1955), Wind stress over a water surface, *Q. J. R. Meteorol. Soc.*, *81*, 639–640.
- Craig, P. D., and M. L. Banner (1994), Modeling wave-enhanced turbulence in the ocean surface layer, *J. Phys. Oceanogr.*, *24*, 2546–2559.
- Conan, P., and C. Millot (1995), Variability of the northern current off Marseilles, western Mediterranean Sea, from February to June 1992, *Oceanol. Acta*, *18*(2), 193–205.
- Courtier, P., C. Freydl, J.-F. Geleyn, F. Rabier, and M. Rochas (1991), The ARPEGE project at Météo-France, in *ECMWF Workshop on Numerical Methods in Atmospheric Modeling*, vol. 2, pp. 193–231, Eur. Cent. for Med.-Range Weather Forecasts, Reading, U. K.
- Cuxart, J., P. Bougeault, and J.-L. Redelsberger (2000), A turbulence scheme allowing for mesoscale and large-eddy simulations, *Q. J. R. Meteorol. Soc.*, *126*, 1–30.
- Donlon, C. J., M. Martin, J. Stark, J. Roberts-Jones, E. Fiedler, and W. Wimmer (2012), The operational sea surface temperature and sea ice analysis (OSTIA) system, *Remote Sens. Environ.*, *116*, 140–158.
- Drobinski, P., et al. (2014), HyMeX, a 10-year multidisciplinary program on the Mediterranean water cycle, *Bull. Am. Meteorol. Soc.*, *95*, 1063–1082, doi:10.1175/BAMS-D-12-00242.1.
- Ducrocq, V., D. Ricard, J.-P. Lafore, and F. Orain (2002), Storm-scale numerical rainfall prediction for five precipitating events over France: On the importance of the initial humidity field, *Weather Forecasting*, *17*, 1236–1256.
- Estournel, C., X. Durrieu de Madron, P. Marsaleix, F. Auclair, C. Julliand, and R. Vehil (2003), Observation and modeling of the winter coastal oceanic circulation in the Gulf of Lion under wind conditions influenced by the continental orography (FETCH experiment), *J. Geophys. Res.*, *108*(C3), 8059, doi:10.1029/2001JC000825.
- Estournel, C., et al. (2016a), High resolution modeling of dense water formation in the North-Western Mediterranean during winter 2012–2013: Processes and budget, *J. Geophys. Res. Oceans*, *121*, 5367–5392, doi:10.1002/2016JC011935.
- Estournel, C., et al. (2016b), HyMeX-SOP2: The field campaign dedicated to dense water formation in the Northwestern Mediterranean, *Oceanography*, *29*(4), 196–206, doi:10.5670/oceanog.2016.94.
- Fouquart, Y., and B. Bonnel (1980), Computations of solar heating of the earth's atmosphere: A new parameterization, *Beitr. Phys. Atmos.*, *53*, 35–62.
- Fourrié, N., et al. (2015), AROME-WMED, a real-time mesoscale model designed for HyMeX special observation periods, *Geosci. Model Dev.*, *8*, 1919–1941, doi:10.5194/gmd-8-1919-2015.
- Gaspar, P., Y. Grégoris, and J.-M. Lefevre (1990), A simple Eddy kinetic energy model for simulations of the oceanic vertical mixing: Tests at station papa and long-term upper ocean study site, *J. Geophys. Res.*, *95*, 16,179–16,193.
- Giordani, H., L. Prieur, and G. Caniaux (2006), Advanced insights into sources of vertical velocity in the ocean, *Ocean Dyn.*, *56*(5–6), 513–524, doi:10.1007/s10236-005-0050-1.
- Giordani, H., G. Caniaux, and A. Voldoire (2013), Intraseasonal mixed-layer heat budget in the equatorial Atlantic during the cold tongue development in 2006, *J. Geophys. Res. Oceans*, *118*, 650–671, doi:10.1029/2012JC008280.
- Giordani, H., C. Lebeaupin Brossier, F. Léger, and G. Caniaux (2017), A PV-approach for dense water formation along fronts: Application to the Northwestern Mediterranean, *J. Geophys. Res. Oceans*, *122*, 995–1015, doi:10.1002/2016JC012019.
- Herrmann, M., and S. Somot (2008), Relevance of ERA40 dynamical downscaling for modeling deep convection in the Mediterranean Sea, *Geophys. Res. Lett.*, *35*, L04607, doi:10.1029/2007GL032442.
- Herrmann, M., F. Sevault, J. Beuvier, and S. Somot (2010), What induced the exceptional 2005 convection event in the north-western Mediterranean basin? Answers from a modeling study, *J. Geophys. Res.*, *115*, C12051, doi:10.1029/2010JC006162.
- Janssen, P. (2004), *The Interaction of Ocean Waves and Wind*, Cambridge Univ. Press, Cambridge, U. K.
- Kolmogorov, A. N. (1942), The equation of turbulent motion in an incompressible fluid, *Izv. Akad. Nauk SSSR, Ser. Fiz.*, *6*, 5658.
- Lazar, A., G. Madec, and P. Delecluse (1999), The deep interior downwelling in the Veronis effect and mesoscale tracer transport parameterizations in an OGCM, *J. Phys. Oceanogr.*, *29*, 2945–2961.
- Lebeaupin Brossier, C., V. Ducrocq, and H. Giordani (2008), Sensitivity of three Mediterranean heavy rain events to two different sea surface fluxes parameterizations in high-resolution numerical modeling, *J. Geophys. Res.*, *113*, D21109, doi:10.1029/2007JD009613.
- Lebeaupin Brossier, C., V. Ducrocq, and H. Giordani (2009), Two-way one-dimensional high-resolution air-sea coupled modelling applied to Mediterranean heavy rain events, *Q. J. R. Meteorol. Soc.*, *135*, 187–204, doi:10.1002/qj.338.
- Lebeaupin Brossier, C., et al. (2014), Ocean mixed layer responses to intense meteorological events during HyMeX-SOP1 from a high-resolution ocean simulation, *Ocean Modell.*, *84*, 84–103, doi:10.1016/j.ocemod.2014.09.009.
- Léger, F., C. Lebeaupin Brossier, H. Giordani, T. Arsouze, J. Beuvier, M.-N. Bouin, E. Bresson, V. Ducrocq, N. Fourrié, and M. Nuret (2016), Dense water formation in the North-Western Mediterranean area during HyMeX-SOP2 in 1/36° ocean simulations: Sensitivity to initial conditions, *J. Geophys. Res. Oceans*, *121*, 5549–5569, doi:10.1002/2015JC011542.
- Lellouche, J.-M., et al. (2013), Evaluation of global monitoring and forecasting systems at Mercator Océan, *Ocean Sci.*, *9*, 57–81, doi:10.5194/os-9-57-2013.
- Lyard, F., F. Lefevre, T. Letellier, and O. Francis (2006), Modelling the global ocean tides: Modern insights from FES2004, *Ocean Dyn.*, *56*(5–6), 394–415.
- Madec, G., and the NEMO team (2008), NEMO ocean engine, in *Note du Pole de Modélisation*, Institut Pierre-Simon Laplace (IPSL), Paris.
- Madec, G., P. Delecluse, M. Imbard, and C. Levy (1998), OPA8 ocean general circulation model—Reference manual, LODYC/IPSL Note 11, Institut Pierre Simon Laplace des sciences de l'Environnement Global, Paris.
- Marshall, J., and F. Schott (1999), Open-ocean convection: Observations, theory, and models, *Rev. Geophys.*, *37*, 1–64.
- Masson, V. (2000), A physically-based scheme for the urban energy budget in atmospheric models, *Boundary Layer Meteorol.*, *94*, 357–397.
- Masson, V., et al. (2013), The SURFEXv7.2 land and ocean surface platform for coupled and offline simulation of earth surface variables and fluxes, *Geosci. Model Dev.*, *6*, 929–960, doi:10.5194/gmd-6-929-2013.
- Millot, C. (1999), Circulation in the Western Mediterranean Sea, *J. Mar. Syst.*, *20*(14), 423–442.
- Millot, C., and I. Taupier-Letage (2005), Circulation in the Mediterranean Sea, in *The Mediterranean Sea, Handbook Environ. Chem.*, vol. 5, edited by A. Salot, pp. 29–66, Springer, Berlin, Germany, doi:10.1007/b107143.
- Mlawer, E. J., S. J. Taubman, P. D. Brown, M. J. Iacono, and S. A. Clough (1997), Radiative transfer for inhomogeneous atmospheres: RRTM, a validated correlated-k model for the longwave, *J. Geophys. Res.*, *102*, 16,663–16,682.

- Noilhan, J., and S. Planton (1989), Simple parameterization of land surface processes for meteorological models, *Mon. Weather Rev.*, *117*, 536–549.
- Olabarrieta, M., J. C. Warner, B. Armstrong, J. B. Zambon, and R. He (2012), Ocean-atmosphere dynamics during hurricane Ida and nor'Ida: An application of the coupled ocean-atmosphere-wave-sediment transport (COAWST) modeling system, *Ocean Model.*, *43–44*, 112–137, doi:10.1016/j.ocemod.2011.12.008.
- Pergaud, J., V. Masson, S. Malardel, and F. Couvreur (2009), A parameterization of dry thermals and shallow cumuli for mesoscale numerical weather prediction, *Boundary Layer Meteorol.*, *132*, 83–106.
- Pinty, J.-P., and P. Jabouille (1998), A mixed-phased cloud parameterization for use in a mesoscale non-hydrostatic model: Simulations of a squall line and of orographic precipitation, in *Conference on Cloud Physics*, pp. 217–220, Am. Meteorol. Soc., Everett, Wash.
- Pullen, J., J. D. Doyle, and R. P. Signell (2006), Two-way air-sea coupling: A study of the Adriatic, *Mon. Weather Rev.*, *134*, 1465–1483.
- Rainaud, R., C. Lebeaupin Brossier, V. Ducrocq, H. Giordani, M. Nuret, N. Fourrié, M.-N. Bouin, I. Taupier-Letage, and D. Legain (2016), Characterization of air-sea exchanges over the Western Mediterranean Sea during HyMeX SOP1 using the AROME-WMED model, *Q. J. R. Meteorol. Soc.*, *142*(S1), 173–187, doi:10.1002/qj.2480.
- Renault, L., J. Chiggiato, J. C. Warner, M. Gomez, G. Vizoso, and J. Tintoré (2012), Coupled atmosphere-ocean-wave simulations of a storm event over the Gulf of Lion and Balearic Sea, *J. Geophys. Res.*, *117*, C09019, doi:10.1029/2012JC007924.
- Ricchi, A., M. M. Miglietta, P. P. Falco, A. Benetazzo, D. Bonaldo, A. Bergamasco, M. Sclavo, and S. Carnier (2016), On the use of a coupled ocean-atmosphere-wave model during an extreme cold air outbreak over the Adriatic Sea, *Atmos. Res.*, *172–173*, 48–65, doi:10.1016/j.atmosres.2015.12.023.
- Roullet, G., and G. Madec (2000), Salt conservation, free surface and varying levels: A new formulation for ocean general circulation models, *J. Geophys. Res.*, *105*, 23,927–23,942, doi:10.1029/2000JC900089.
- Schott, F., M. Visbeck, U. Send, J. Fischer, L. Stramma, and Y. Desaubies (1996), Observations of deep convection in the Gulf of Lion, Northern Mediterranean, during the winter of 1991/1992, *J. Phys. Oceanogr.*, *26*, 505–524.
- Seity, Y., P. Brousseau, S. Malardel, G. Hello, P. Bénard, F. Bouttier, C. Lac, and V. Masson (2011), The AROME-France convective scale operational model, *Mon. Weather Rev.*, *139*, 976–991.
- Small, R. J., T. Campbell, J. Teixeira, S. Carniel, T. A. Smith, J. Dykes, S. Chen, and R. Allard (2011), Air-sea interaction in the Ligurian Sea: Assessment of a coupled ocean-atmosphere model using in-situ data from LASIE07, *Mon. Weather Rev.*, *139*, 1785–1808, doi:10.1175/2010MWR3431.1.
- Small, R. J., S. Carniel, T. Campbell, J. Teixeira, and R. Allard (2012), The response of the Ligurian and Tyrrhenian Seas to a summer mistral event: a coupled atmosphere-ocean approach, *Ocean Modell.*, *48*, 30–44.
- Somot, S., et al. (2016), Characterizing, modelling and understanding the climate variability of deep water formation in the North-Western Mediterranean Sea, *Clim. Dyn.*, 1–32, doi:10.1007/s00382-016-3295-0.
- Taillefer, F. (2002), CANARI (code for the analysis necessary for ARPEGE, for its rejects and its initialization): Technical documentation, technical report, CNRM/GMAP, Météo-France, Toulouse, France. [Available at <http://cnrm.meteo.fr/gmapdoc/spip.php?article3>]
- Testor, P., et al. (2017), Multi-scale observations of deep convection in the northwestern Mediterranean Sea during winter 2012–2013 from a multi-platform approach, *J. Geophys. Res. Oceans*, doi:10.1002/2016JC012671, in press.
- Valcke, S., T. Craig, and L. Coquart (2013), OASIS3-MCT user guide, *Tech. Note TR/CMGC/13/17*, CERFACS, Toulouse, France.
- Voltaire, A., et al. (2017), The seamless and multi-model coupling between atmosphere, land, hydrology, ocean, waves and sea-ice models based on SURFEX v8 surface model using OASIS3-MCT, *Geosci. Model Dev.*, doi:10.5194/gmd-2017-91, in press.
- Waldman, R., et al. (2016), Estimating dense water volume and its evolution for the year 2012–2013 in the Northwestern Mediterranean Sea: An observing system simulation experiment approach, *J. Geophys. Res. Oceans*, *121*, 6696–6716, doi:10.1002/2016JC011694.
- Warner, J. C., B. Armstrong, R. He, and J. B. Zambon (2010), Development of a Coupled Ocean-Atmosphere-Wave-Sediment Transport (COAWST) modeling system, *Ocean Modell.*, *35*, 230–244.